iPSC-derived *NF1-CDKN2A*-PRC2 deficient neural crest cells mimic glial-to-neuro-mesenchymal transition and form MPNST-like tumors in vivo

Itziar Uriarte-Arrazola[1], Míriam Magallón-Lorenz[2], Juana Fernández-Rodríguez[3,4,5,6], Judit Farrés-Casas[1], Sara Ortega-Bertran[3,4], Edgar Creus-Bachiller[3,4], Cleofé Romagosa[7], Conxi Lázaro[3,4,6], Helena Mazuelas[1], Bernat Gel[2,8,***], Meritxell Carrió[1,#,**] & Eduard Serra[1,6,#,*]

1) Hereditary Cancer Group, CARE Program; Germans Trias i Pujol Research Institute (IGTP) Badalona, Barcelona, 08916; Spain
2) Translational Bioinformatics and Genomics of Cancer, CARE Program; Germans Trias i Pujol Research Institute (IGTP) Badalona, Barcelona, 08916; Spain
3) Hereditary Cancer Program, Catalan Institute of Oncology (ICO-IDIBELL), L'Hospitalet de Llobregat, Barcelona, 08098; Spain
4) Program in Molecular Mechanisms and Experimental Therapy in Oncology (Oncobell), IDIBELL, Hospitalet de Llobregat, Barcelona, Spain
5) Mouse lab, SCT-IDIBELL, Hospitalet de Llobregat, Barcelona, Spain
6) Centro de Investigación Biomédica en Red de Cáncer (CIBERONC), Spain
7) Pathology Department, Hospital Universitari Vall d'Hebron, Barcelona, Spain
8) Departament de Fonaments Clínics, Facultat de Medicina i Ciències de la Salut, Universitat de Barcelona (UB), 08036, Barcelona, Spain.

Last authors
*, **, *** Corresponding authors: eserra@igtp.cat; mcarriol@igtp.cat; bgel@igtp.cat
Lead contact: eserra@igtp.cat

Abstract
Neurofibromatosis Type 1 (NF1) predisposes to peripheral nerve tumor development. Commonly, the progression from a benign plexiform neurofibroma (PNF) towards a deadly malignant peripheral nerve sheath tumor (MPNST) involves a poorly understood glial-to-mesenchymal transition and the sequential loss of *NF1*, *CDKN2A*, and polycomb repressive complex 2 (PRC2). Using an iPSC-derived neural crest (NC) model, we reproduced this malignant transformation. *NF1-CDKN2A* double-knockout (2KO) NCs retained glial differentiation capacity and generated neurofibroma-like tumors *in vivo*, requiring inactivation of p14ARF and p16INK4A. Additional PRC2 loss (3KO) disrupted pluripotency and induced mesenchymal stem cell-like features. 3KO NC globally reassembled chromatin accessibility, impeding gliogenesis by *SOX10* epigenetic silencing and activating neuro-mesenchymal programs by chromatin opening, reinforced in MPNSTs. This glial-to-neuro-mesenchymal transition recapitulated neurofibroma-to-MPNST progression, since 3KO NC spheres formed MPNST-like tumors *in vivo*, genuinely mimicking early-stage MPNST development. This iPSC-based model constitutes a platform for studying the molecular pathogenesis of NF1-associated sarcomagenesis and therapeutic discovery.

Keywords: MPNST, plexiform neurofibroma, ANNUBP, Neurofibromatosis Type 1, *NF1*, *CDKN2A*, polycomb repressive complex 2 (PRC2), Neural Crest, iPSC, 3D model.

INTRODUCTION

Malignant peripheral nerve sheath tumors (MPNSTs) are soft tissue sarcomas that arise from cells of the peripheral nerve sheath (PNS). Around 45% of MPNSTs are associated with Neurofibromatosis type 1 (NF1), an inherited cancer predisposition syndrome characterized by the development of benign and malignant tumors of the PNS. Another 45% of MPNSTs arise sporadically in the general population and the remaining 10% is associated to previous radiotherapy treatment.[1,2] MPNSTs account for 3-10% of all soft tissue sarcomas.[3] NF1 patients have a 10-15% lifetime risk of developing an MPNST,[4,5,6] which are their primary cause of death.[4,7,5,8] These malignant tumors are characterized by an aggressive behavior and high tendency to metastasize, typically spreading to the brain, bones, and lungs. The 5-year survival rate is poor, particularly in the NF1 context.[4,9] As with many other soft tissue sarcomas, complete surgical removal with clear margins is critical for effective management, often followed by radiotherapy and/or chemotherapy.[10,11,12]

In the NF1 context, MPNST normally develop through an initial loss of several tumor suppressor genes (TSGs) in a stepwise manner.[13,14,15,16,17,18,19,20] During development, a benign plexiform neurofibroma (PNF) may arise in large nerves, originating from a precursor cell within the Neural Crest (NC)-Schwann cell (SC) lineage, after the complete inactivation of *NF1*.[21] The additional loss of the complete *CDKN2A* locus, forms a distinct nodular pre-malignant lesion termed an atypical neurofibromatous neoplasm of uncertain biological potential (ANNUBP). Both lesions share a predominant glial component but with a different cell microenvironment. The transition toward MPNST involves the loss of polycomb repressive complex 2 (PRC2), a chromatin remodeler complex driving transcriptional repression during development,[22] through inactivation of its components *SUZ12* or *EED*.[23,2] This transition is also concurrent with a shift towards a mesenchymal identity, with the loss of glial markers such as SOX10 or S100B.[24,25,26] *TP53* is also frequently lost in MPNSTs, but at a lesser extent compared to *NF1*, *CDKN2A* and PRC2.[2,27,28] In addition to these initial TSG losses, MPNST genome undergoes a extensive genomic reorganization, usually resulting in hyperploid genomes and involving many copy number and structural changes. Conversely, mutational burden is low and there are no specific mutational signatures.[29,30]

Several *in vitro* and *in vivo* models have been developed for PNF, ANNUBP and MPNST, associated with NF1, to study their biology and identifying potential new therapies.[31,32] However, only few models may mimic the progression from benign to malignant tumors.[33,34,35]

In this work, we aimed to explore the biological impact of *NF1*, *CDKN2A* and PRC2 loss on MPNST development. For that, we used an iPSC-derived 3D neurofibroma model previously developed in our lab.[36,37] Using CRISPR-based gene editing, we inactivated *CDKN2A* and *SUZ12* to reproduce the sequential loss of TSGs in the PNF-ANNUBP-MPNST progression path and characterized the impact of losing these TSGs in cell function and identity. The resulting models captured the glial-to-mesenchymal transition characteristics of neurofibroma-to-MPNST transformation, with triple-knockout (*NF1*, *CDKN2A*, PRC2) NC spheres forming early-stage MPNSTs when orthotopically engrafted into the sciatic nerve of nude mice.

RESULTS

In vivo neurofibroma-like tumor formation of *NF1*(-/-) *CDKN2A*(-/-) neurofibromaspheres requires the loss of p14^{ARF}

We first aimed to inactivate *CDKN2A* in a *NF1*(-/-) iPSC line (1KO_D12).[36] *CDKN2A* locus encodes two proteins, p14ARF (p14) and p16INK4A (p16), partially sharing exonic regions but in a different reading frame. We designed two different CRISPR-Cas9 editing strategies targeting exon 2 using specific sgRNAs: one designed to selectively disrupt p16, and the other one inactivating both p14 and p16 (Figure 1A). We successfully generated two *NF1*(-/-) *CDKN2A* p16(-/-) (2KO (p16)), and three *NF1*(-/-) *CDKN2A* p14p16(-/-) (2KO (p14p16)), iPSC lines (Figure S1A and File S1). The generation and expansion of clones with p16 inactivated and p14 WT was much less efficient than with both proteins inactivated. In fact, one of the two 2KO (p16) iPSC lines (2KO_A11) obtained, displayed an abnormal phenotype, slow proliferation behavior and loss of pluripotency (Figure S1B). We confirmed both, newly CRISPR generated mutations at *CDKN2A* and previous *NF1* pathogenic variants, by sanger sequencing (File S1) and by western blot (Figure S1C, S1D). iPSC lines were characterized by pluripotency marker expression (OCT3/4) and their ability to differentiate into homogeneous populations of NC cells, as assessed by cytometry analysis (p75 and Hnk1) and immunocytochemistry (TFAP2 and SOX10) (Figure 1B). p16 is detected by western blot at the level of NC but not at iPSC. Thus, after the generation and genotype confirmation of 2KO iPSCs, we characterized the impact of *CDKN2A* loss on NC physiology. Since *CDKN2A* is associated with cell cycle control, we performed proliferation and ploidy assays (Figure S1E, S1F), but no differences were observed compared to the parental 1KO cell line, only deficient in *NF1*. Whole-genome sequencing (WGS) confirmed an isogenic diploid (2n) genome without structural or any other relevant alterations of the 2KO_F9 (p14p16) cell line used for subsequent analysis (Figure S1G).

We then tested the tumor formation capacity of 2KO (p16) and 2KO (p14p16) cell lines. We generated neurofibromaspheres by differentiating NCs towards cells of the Schwann cell (SC) lineage, and mixed them with primary neurofibroma fibroblasts allowing them to form spheres for up to 14 days (Figure 1C, 1D).[37] Spheres were engrafted into the sciatic nerve of nude mice, and 4 months later, mice were sacrificed to assess tumor formation. The 1KO cell line generated tumors in 10 out of 15 injections, whereas the 2KO (p14p16) cell line formed tumors in 9 out of 15 injections. Histological analysis by H&E and S100B immunostaining confirmed a genuine neurofibroma-like morphology in both genotypes, with no evident differences between them. Ku80 staining confirmed the human origin of S100B positive cells (Figure 1E). In contrast, 2KO (p16) spheres, displayed markedly reduced tumorigenic potential, with few outgrowths detected in only 3 out of 15 injections, and when formed, they were significantly smaller than those derived from 1KO and 2KO (p14p16) cell lines. Altogether, these results indicated that while 2KO (p14p16) spheres formed genuine neurofibroma-like tumors, with no apparent histological differences compared to 1KO tumors, the presence of wild-type p14 in partially inactivated 2KO cell lines (2KO p16), impairs proper neurofibroma formation.

2KO NC are sensitive to thymidylate synthase inhibition

Next, we interrogated the impact of *CDKN2A* loss on overall expression. We performed RNA-seq of biological triplicates of 1KO and 2KO (p14p16) at iPSC and NC stage, and performed a principal component analysis (PCA) (Figure 1F). p14 and p16 loss had a clear impact on gene expression. We identified several differentially overexpressed genes in 2KO cells compared to 1KO, shared by iPSCs and NCs. 71 of these genes were also differentially expressed when comparing PNFs and ANNUBPs (Figure 1G and File S2). However, in ANNUBPs, 2KO cells may account for less than 50% of tumor cells,[18] and only three of the 71 genes were found to be overexpressed in ANNUBPs, two of them being related to immune infiltrate. The third overexpressed gene was *TYMS*, encoding for thymidylate synthase (TS) (Figure 1H). The described synthetic lethality between loss of *CDKN2A* and TS inhibition[38] prompted us to test the sensitivity of 2KO NC cells to TS inhibitors compared to 1KO NCs. We used the TS inhibitor Pemetrexed on 1KO and 2KO NC cultures (Figure 1I-1K) and observed a significantly higher sensitivity of 2KO NCs to *TYMS* inhibition (Figure 1I, 1J). Although senescence was ruled out as the cause of this sensitivity, we observed marked morphological changes in the cells, including increased size, aberrant nuclei, and enlarged cytoplasm in 2KO cells (Figure 1K).

Inactivation of *NF1*, *CDKN2A* and PRC2 in iPSCs exhibit a biologically imposed order

Next step involved the inactivation of PRC2, through targeted editing of *SUZ12,* in 1KO, 2KO (p16) and 2KO (p14p16) iPSCs. In this step we were able to assess PRC2 functional loss by directly interrogating the absence of the trimethylation of lysine 27 of histone 3 (H3K27me3), using a specific antibody (Figure 2A). We performed multiple transfections in each cell line (Figure 2B) successfully achieving *SUZ12* editing in the three genotypically distinct iPSCs (Figure 2C). However, when trying to expand the different edited clones, we were not able to succeed for 1KO and 2KO (p16), that is, for those iPSCs with preserved p14ARF function (Figure S2A, S2B). Contrarily, we indeed were able to expand clones from 2KO (p14p16) edited iPSCs and perpetuate them at the NC stage (see below), obtaining 3KO cell lines with no functional *NF1*, *CDKN2A* (p14p16) and *SUZ12* (Figure 2B, 2D). These results suggested that the order of TSG inactivation in *NF1*(-/-) iPSCs required a biologically imposed specific sequence: first the complete inactivation of the *CDKN2A* locus (involving p14 and p16) and then the loss of PRC2.

To confirm these findings, we tested the re-expression of either p14 or p16 in 2KO (p14p16) and 3KO cell lines, at NC stage. For that, we used lentiviral vectors carrying bicistronic expression cassettes consisting in either p16 and mCherry or p14 and GFP, under the expression of a doxycycline-inducible promoter (Figure 2E). We designed an experiment (Figure 2F) that allowed us to assess the percentage of cells either mCherry (p16) or GFP (p14) positive, after doxycycline induction. Transduced and selected cells were induced with doxycycline and the percentage of fluorescent cells was analyzed 5 and 8 days later. To control for any potential decay in fluorescence due to lentiviral silencing, we compared the percentage of fluorescent cells after 24h doxycycline induction at the beginning of the experiment, and after 24h doxycycline induction at 5 and 8 days (Figure 2F). The overall percentage of fluorescent cells was very different between 2KO and 3KO NC lines (Figure 2G) and we attributed this to

different lentiviral silencing in the two genotypes. In 2KO (p14p16) NC cells, the re-expression of p14, somehow equivalent to the 2KO (p16) cell line, had no effect on the viability of initial fluorescent cells (Figure 2Gi). This was consistent with the viability of the 2KO (p16) cell lines. The re-expression of p16 on 2KO (p14p16) NC cells, indeed had a detrimental effect on the viability of initial fluorescent cells (Figure 2Gii). Since we did not generate 2KO (p14) iPSCs, we were not able to demonstrate the potential inability to generate this cell line, as this result suggested. However, we were most interested in the effect of re-expressing p14 and p16 in the 3KO cell lines. p14 re-expression in 3KO cells significantly affected the viability of initial fluorescent cells, with almost no viable fluorescent cells at 8 days (Figure 2Giii). This result was consistent with the inability to expand PRC2 edited 3KO cell lines from 2KO (p16). When we re-expressed p16 in 3KO cells there was also a detrimental effect on the viability of initial fluorescent cells (Figure 2Giv). Altogether these results support the existence of a biologically imposed order of inactivation of TSGs, as in the pNF-ANNUBP-MPNST progression, and support the previous finding that MPNSTs bear the complete inactivation of the *CDKN2A* locus, involving both p14ARF and p16INK4 proteins.[39]

Loss of PRC2 function in *NF1*(-/-) *CDKN2A*(-/-) iPSCs induces loss of pluripotency and acquisition of a mesenchymal identity

After inactivating *SUZ12* in 2KO (p14p16) iPSCs, we expanded clones that lost the H3K27me3. However, under iPSC culture conditions, 3KO clones lost pluripotent morphology and exhibited a gradual spontaneous differentiation, adopting a mesenchymal-like phenotype. In fact, prolonged culture under iPSC media conditions, led to proliferative arrest and the acquisition of a senescent-like state (Figure 3A, 3B). We performed immunostaining on 2KO iPSCs and 3KO cells to confirm all these morphological changes. 2KO iPSC colonies retained H3K27me3 histone mark, denoting PRC2 function, expressed the pluripotency marker OCT3/4 and did not express *SOX9* (Figure 3C). Contrarily, 3KO cells lacked H3K27me3, confirming inactivation of PRC2, lost pluripotency marker expression, and exhibited expression of *SOX9* (Figure 3C). In order to characterize the identity that 3KO cells were adopting, we analyzed mesenchymal stem cell (MSC) markers (CD73, CD13, and CD44) by flow cytometry, confirming the acquisition of mesenchymal stem cell features (Figure 3D). β-galactosidase staining further verified that 3KO cells maintained under iPSC culture conditions eventually stopped proliferating due to senescence (Figure 3E).

3KO neural crest cells recapitulate the glial-to-mesenchymal transition observed in the ANNUBP-MPNST progression

3KO cells were non-viable under standard iPSC culture conditions. Nevertheless, we were able to perpetuate them and establish three independent non-perishable 3KO cell lines by maintaining them under NC culture conditions (Figure 4A-4B, S3A and File S1). Flow cytometry analysis showed that 1KO, 2KO, and 3KO NCs expressed neural crest markers (HNK1, p75). However, 3KO NCs also displayed elevated levels of MSC markers (CD73, CD44, CD13) compared to their 1KO and 2KO counterparts (Figure 4C; Figure S3B). Proliferation rates and ploidy of 3KO NCs remained unchanged compared to 1KO and 2KO NCs, except for 3KO_D8, which exhibited reduced proliferation (Figure S3C, S3D). Notably, this clone also showed the highest expression of MSC markers

(Figure S3B). Furthermore, all 3KO NC cell lines exhibited an unaltered 2n genome like their parental 2KO cell line, as assessed by WGS analysis (Figure S3E), suggesting that the loss of PRC2 was not sufficient to drive genomic alterations normally observed in MPNSTs, at least, after several cell culture passages. These findings indicated that 3KO NCs acquire a mixed NC-MSC identity.

To better characterize the impact of losing PRC2 function in NCs, we performed bulk RNA-Seq of 1KO, 2KO, and 3KO NCs, in three independent biological replicates. We selected different glial and mesenchymal markers and observed that 3KO NCs exhibited a drastic downregulation of glial genes (*SOX10*, *NGFR*, *PLP1*), and an upregulation of mesenchymal markers (*SOX9*, *TWIST1*, *PRRX1*) (Figure 4D). To understand the relevance of this finding in the context of the glial-to-mesenchymal transition that occurs in the ANNUBP to MPNST progression, we analyzed single-cell RNA-seq data from nerves, PNFs, ANNUBPs, and MPNSTs, to analyze the observed transcriptional changes (Figure 4E). *SOX10*, *NGFR* and *PLP1* expression was restricted to the glial component of all tissues and tumors analyzed together, particularly expressed in ANNUBP samples. Contrarily, *SOX9*, *TWIST1* and *PRRX1* expression was restricted to the mesenchymal component of the single cell analysis, mainly expressed in the MPNST samples (Figure 4E). Notably, immunofluorescence analysis of *SOX10* and *SOX9*—key NC transcription factors—revealed an inverse relationship across 1KO, 2KO, and 3KO NCs: while SOX10 expression gradually diminished and was absent in 3KO NCs, SOX9 reached a maximum protein expression in these cells. (Figure 4F and Figure S3F).

Whole-transcriptome differential expression analysis identified a set of downregulated genes in 3KO NCs compared to 2KO NCs (Figure 4G and File S3). Enrichment analysis of all significantly downregulated genes identified gliogenesis-related biological processes among those inhibited in 3KO cells (Figure 4H and File S3). To determine whether this inhibition was a direct consequence of an epigenetic change produced by PRC2 loss, we performed ATAC-seq analysis of 1KO, 2KO and 3KO NCs. Several downregulated gliogenesis-associated genes in 3KO NCs were associated with closed chromatin states compared to 1KO and 2KO NCs. Among them was the gliogenesis master regulator *SOX10*, indicating its transcriptional silencing through chromatin compaction (Figure 4I), reinforcing the downregulation of gliogenesis-related genes. In contrast, *SOX9* transcription factor remained under an open conformation of the chromatin in 3KO NC cells (Figure S3G).

Finally, we functionally evaluated the ability of 3KO NCs to differentiate towards SCs. SC differentiation was induced in 1KO, 2KO, and 3KO NCs for 21 days;[40] only 1KO and 2KO cells showed expression of SC markers (p75 and S100B), in contrast to 3KO cells (Figure 4J). These results further emphasized the loss of glial differentiation capacity and the acquisition of a mesenchymal identity upon inactivation of PRC2 function in 3KO NC cells, recapitulating the transition observed in ANNUBP to MPNST progression.

3KO NC spheroids generate human MPNST-like tumors upon nerve engraftment in nude mice

Neurofibromaspheres derived from 1KO and 2KO NCs generate neurofibroma-like tumors when engrafted in the sciatic nerve of nude mice[36] (Figure 1E). We performed a tumor formation assay by engrafting 3KO NC-like spheroids in contact with the sciatic nerve of nude mice (Figure 5A). After four months, mice were sacrificed. We identified

large, highly nucleated human tumors at the injection site and adjacent to the nerve. These tumors exhibited numerous mitotic figures detectable by H&E staining, as assessed by an expert pathologist in NF1 (Figure 5A). We confirmed the human origin of these cells by Ku-80 staining (Figure 5A). Alongside 3KO NC spheres, we also engrafted 1KO and 2KO neurofibromaspheres for a comparative analysis. We analyzed the expression of several markers, including H3K27me3, SOX10, S100B, vimentin, and Ki67 (Figure 5B). As expected, tumors derived from 1KO and 2KO spheroids retained H3K27me3 expression, whereas 3KO tumors were negative, confirming PRC2 loss. Moreover, 1KO and 2KO tumors expressed SOX10 and S100B glial markers, consistent with a neurofibroma-like identity. In contrast, 3KO tumors lost the expression of these markers (Figure 5B). All tumor types expressed vimentin and stained positive for Ki67, indicative of tumorigenesis, fibrosis, and proliferative activity (Figure 5B). The expression of these two markers was slightly higher in 3KO tumors, suggesting an increased proliferation rate. Taken together, these findings confirmed that 3KO NCs spheres were able to generate early-stage MPNSTs, in contrast to human and mouse *NF1* deficient NCs that cannot form any tumor,[36,41] providing a robust model for studying MPNST progression and for *in vitro* and *in vivo* therapeutic screening.

MPNST cell identity is highly impacted by PRC2 inactivation and MSC-like features

3KO NC cells represent a valuable model of the early stages of MPNST development. However, after an initial TSG loss, MPNST cells undergo a genome rearrangement event, eventually giving rise to a viable rewired cancerous cell. We compared 3KO NCs, representing an early MPNST stage, with established MPNST cell lines, representing a late MPNST stage, to identify the molecular MPNST features present or still absent in the 3KO NC model. We focused on how PRC2 loss and the acquisition of a mesenchymal identity shape the phenotype of MPNST cells (Figure 6A).

For that, we first differentiated 3KO NC lines and their parental 2KO, 1KO and WT isogenic NC lines into mesenchymal stem cells (MSCs) (Figure 6B and Figure S4A). Differentiating 3KO NCs into MSCs led to early proliferative arrest and senescence (Figure S4B), preventing the generation of a stable 3KO MSC model. However, sufficient MSCs were obtained to enable multiple downstream analyses. We included all different genotypes and cell identities, from iPSCs to NC and MSCs, and also five MPNST cell lines bearing the inactivation of the 3 TSGs (Figure 6B).

We performed transcriptome (RNA-seq) for all cell types; methylome (EPIC array) for NCs, MSCs and MPNST cell lines and chromatin accessibility analysis (ATAC-seq) for NCs. PCAs evidenced a profound contribution of both PRC2 loss and MSC expression in defining the identity of MPNST cell lines, with a clear impact of both factors on transcriptome and methylome profiles (Figure 6Ci, 6Cii). In addition, the loss of PRC2 also had a profound effect on chromatin accessibility in NCs, as expected (Figure 6Ciii).

To investigate the genes and biological processes contributing to MPNST cell identity driven by PRC2 loss and the acquisition of a mesenchymal identity we performed two types of differential expression analyses. We first compared 2KO and 3KO NC cell lines to account for PRC2 function at NC level and plotted differentially expressed genes in a heatmap with MPNST cell lines and all genotypes of NC and MSC (Figure 6D and File S4). As expected, unsupervised cluster analysis clearly separated samples in two groups, those retaining wild-type PRC2 function and those PRC2-deficient. Notably, we identified a set of overexpressed genes (Cluster 1) shared by MPNST cell lines, 3KO

MSCs and 3KO NCs, indicating that these genes are preferentially upregulated in PRC2-deficient cell lines. Enrichment analysis of Cluster 1 revealed numerous biological processes associated with neurogenesis (Figure 6E and File S4). To elucidate the key features that 3KO NCs (early-stage MPNST model) need to acquire to resemble established MPNST cell lines (late-stage model), we compared both cell types (Figure 6F). Differentially expressed genes were plotted in a heatmap. Here, unsupervised clustering clearly separated cell lines with NC identity, from those with a mesenchymal cell identity, like MSCs and MPNST cell lines, regardless of their genotype (Figure 6F and FileS5). We identified a set of genes overexpressed only in cell lines with mesenchymal identity (Cluster 2). Enrichment analysis of cluster 2 revealed multiple terms associated with mesenchymal identity, including 73 genes involved in wound healing (Figure S4C and File S5), a term potentially related to the aggressiveness of solid tumors.[42] At the NC stage, most of these genes had a differentially open chromatin conformation in 3KO NC compared to 2KO NCs (Figure S4D) but many were not differentially expressed, probably requiring the acquisition of additional mesenchymal features to change their expression levels (Figure S4E). We selected individual genes like *PLEC* and *PPARG* to illustrate some examples of chromatin accessibility and bulk expression (Figure S4F). Single cell RNA-seq data revealed their expression in MPNSTs and not in nerves, PNF or ANNUBP tissues (Figure S4G). Furthermore, we identified an additional group of genes overexpressed only in MPNST cell lines (Cluster 3, Figure 6F). Interestingly, an enrichment analysis of this cluster revealed biological processes also related to neurogenesis (Figure 6G and File S5). These findings indicate that neurogenesis-related gene signatures are not only induced in 3KO cells as a consequence of PRC2 loss, but are further reinforced in MPNST cell lines by the expression of additional neurogenesis genes.

Expression of neurogenesis genes as part of MPNST cell identity

To obtain a global sense of the importance of neurogenesis gene signatures in the identity of MPNST cells, we performed a global analysis of neurogenesis gene expression together with their chromatin accessibility status. Expression analysis of Cluster 1 genes associated with neurogenesis-related biological processes (Figure 6D, 6E) showed a consistent high expression across all 3KO cell lines—3KO NCs, 3KO MSCs and MPNST cell lines (Figure 7A). To analyze whether this gene expression resulted from the opening of the chromatin triggered by PRC2 loss, we performed a differential chromatin accessibility analysis based on ATAC-seq data, comparing PRC2 WT NCs (1KO, 2KO) with PRC2 inactivated cell lines (3KO). We plotted the differential chromatin accessibility data for all genes differentially expressed between 2KO NC and 3KO NCs, highlighting those associated with neurogenesis within Cluster 1 (Figure 7B). Most neurogenesis-associated genes displayed a more open chromatin conformation in 3KO NCs. We then visualized the correlation between differential chromatin accessibility and differential gene expression, highlighting Cluster 1 neurogenesis genes (Figure 7C) and showed that most of these genes are immediately overexpressed in 3KO NCs upon a more accessible open chromatin conformation. We selected individual genes like *PITX1* (Figure 7D) and *PCSK1* (Figure 7E) to illustrate chromatin accessibility and expression status. For *PCSK1* we also obtained scRNA-seq data, indicating that this gene is expressed essentially in MPNST cells, but not in nerves, PNF or ANNUBP glial component (Figure 7E).

We next applied the same analysis for Cluster 3 neurogenesis-associated genes, identified through the comparison between 3KO NCs and MPNST cell lines (Figure 6F). Here, the global expression analysis indicated a differential overexpression of Cluster 3 neurogenesis genes in MPNST cell lines (Figure 7F). Despite these genes being transcriptionally silent in 3KO NCs, we interrogated their chromatin conformation status and found that Cluster 3 neurogenesis genes also displayed an open chromatin conformation due to PRC2 loss (Figure 7G). The correlation between gene expression and ATAC-seq data confirmed this uncoupling (Figure 7H). Although some specific genes were indeed overexpressed, most genes remained unchanged in expression (Figure 7H) when chromatin opened. In fact, within Cluster 3, neurogenesis genes exhibited three types of behavior (Figure 7I-7K and Figure S5): genes whose expression starts at 3KO NCs but highly increases in MPNST cell lines (Figure 7I, Figure S5A); genes that are exclusively expressed at 3KO MSCs and MPNST cell lines (Figure 7J, Figure S5B); and lastly, genes that are only expressed in MPNST cell lines (Figure 7K, Figure S5C). These results suggest that while loss of PRC2 opens chromatin accessibility of most neurogenesis genes, some still require an MSC-like identity to be expressed in MPNSTs, and some require additional factors only present in MPNST cell lines. Finally, Cluster 2 genes (Figure 6F) exhibited a relationship between expression and epigenetic status closely resembling Cluster 3 neurogenesis genes, but showing a greater heterogeneity (Figure S4D, S4E).

Overall, results supported that NF1-associated 3KO MPNST identity is deeply influenced by losing glial differentiation capacity and the expression of developmental neuro-mesenchymal programs. To complete this view, we plotted together gliogenesis (Figure 4G) and neurogenesis (Figure 6C, 6G) genes, in the graph correlating gene expression and chromatin accessibility. While the former are downregulated, partly by epigenetic silencing, the latter are predominantly upregulated in an open chromatin conformation (Figure 7L). This view was supported by an independent enrichment analysis of differential chromatin accessibility between 2KO and 3KO NCs (Figure 7M).

To conclude, we aimed to translate the relevance of the discoveries made using our iPSC-derived NC models, to NF1-associated tumors. We took bulk RNA-seq data from primary PNF-derived SCs, PNFs, ANNUBPs and MPNSTs, and plotted the expression of all gliogenesis and neurogenesis genes previously identified (Figure 7N). The gliogenesis cluster was mainly expressed in PNF-derived SCs, and benign tumors (PNF and ANNUBP). Neurogenesis genes from Cluster 1, could be divided in three groups: one heterogeneous group of genes (*NGF*, *VIM*, *ITGA2* and others) was upregulated in benign tumors and SCs; another group of genes (*FOXD1*, *GATA3*, *PCSK1* and others) was upregulated in MPNSTs, completely absent in PNF-derived SCs, had some expression in PNFs and a bit less in ANNUBPs with their expression probably coming from fibroblasts and other stromal cells; finally, the last group of genes (*NKX2-2*, *PITX1*, *FOXG1* and others), like most genes in Cluster 3 (for example *NR2E1*, *DMRT3*, *FOXB1*), were overexpressed in MPNSTs only. This heatmap shows that the glial-to-neuro-mesenchymal transition gene signatures identified with our NC models illustrate the benign-to-malignant transition seen in NF1-related PNS tumors.

DISCUSSION

We studied the role of most commonly inactivated TSGs in the early development of MPNSTs. For that, we used an iPSC-derived NC model system and sequentially inactivated these TSGs (*NF1*, *CDKN2A* and *SUZ12*), as it happens in the benign-malignant transition of PNF-ANNUBP-MPNST progression (Figure 8).

It is now well established that the loss of *CDKN2A* in *NF1*(-/-) PNF cells is the trigger of ANNUBP formation,[15,18,19] becoming a premalignant lesion difficult to clinically manage due to the lack of tools for risk assessment. [16,17,43] In our NC model, 2KO NCs retain glial differentiation capacity and form neurofibroma-like lesions when engrafted in the sciatic nerve of nude mice. However, no histological atypia was detected in these neurofibromas, suggesting that a longer period of tumor development might be necessary. *CDKN2A* inactivation in 2KO NCs did not affect the cell cycle or proliferation rate, but led to gene expression changes when compared to 1KO NCs. One of the differentially expressed genes was *TYMS* which is also differentially overexpressed in ANNUBPs compared to PNFs. *TYMS* inhibitors, like Pemetrexed, exist and have been used to inhibit proliferation in cells deficient in *CDKN2A.*[38] Our results show the existence of a window of opportunity for *TYMS* inhibition in ANNUBPs, although further experiments are required to confirm this possibility.

CDKN2A is a complex gene locus encoding for two proteins, p14ARF and p16INK4A, partially sharing exonic regions but using a different reading frame. Different genetically modified mouse (GEM) models demonstrated the loss of *NF1* and *CDKN2A* for ANNUBP formation,[34,35] some pointing to p14ARF as the key *CDKN2A* gene. Our model supports the necessity of losing both p14ARF and p16INK4A for the proper development of ANNUBP. In fact, loss of both genes is found in human MPNST and MPNST cell lines.[30,39] Results presented here demonstrate that wild-type p14ARF function impeded the proper formation of tumors *in vivo,* but overall support the need for the double inactivation of p14ARF and p16INK4A for progression towards an MPNST.

PRC2 plays essential roles during development by catalyzing histone H3 lysine 27 tri-methylation (H3K27me3) and in this way, determining chromatin accessibility.[44] PRC2 function helps maintain cell identity basically through transcriptional repression and has been involved in many types of cancer.[22] In MPNSTs, PRC2 acts as a TSG,[23] is lost in a large number of MPNSTs,[2] although not in all cases (Magallón-Lorenz unpublished data),[20] likely contributing to the pathological heterogeneity observed among MPNSTs. Our work supports that the order of TSG inactivation in the PNF-ANNUBP-MPNST progression is biologically constrained. Indeed, if either p14ARF or p16INK4A genes remained functional in an *NF1*(-/-) background, the absence of PRC2 made iPSC cells not viable. In *NF1* patients carrying a constitutional microdeletion involving the *NF1* gene and other additional genes including *SUZ12*, their neurofibromas never exhibit LOH encompassing *NF1* and *SUZ12* as a *second hit*.[45] We are tempted to speculate that this could be due to the same observed biological constraint: PRC2 loss would activate p14ARF/p16INK4A expression through chromatin accessibility, inducing senescence[46,47]. An exception to this imposed order could be in the group of MPNSTs that inactivate *TP53* after *NF1*, and before PRC2 (Magallón-Lorenz unpublished data).[20]

In our hands, upon *SUZ12* removal, 3KO iPSCs lost pluripotency and underwent spontaneous differentiation, in accordance with current knowledge.[44,48] 3KO cells were viable and acquired a stable identity if, after PRC2 loss, they were maintained under

NC culture conditions (Figure 8). To the best of our knowledge, this is the first iPSC-based tumor model that captures a benign-to-malignant transition, occurring with a change in cell identity after the inactivation of the chromatin remodeler PRC2. Mimicking the glial-to-mesenchymal transition observed from ANNUBP towards MPNST, 3KO NCs acquired a mesenchymal identity, consistent with previous results.[49] Other works have studied the role of PRC2 in the acquisition of mesenchymal characteristics, by comparing MPNSTs with proficient and deficient PRC2, or re-expressing or deleting their components in MPNST or immortalized SC cell lines.[24,25,26] Instead, we have been able to start from a cell type at an earlier differentiation stage than the cells originating MPNSTs. This has allowed us to reproduce the loss of TSGs occurring during malignant transformation in a cell type close to the cell of origin and dissect the molecular basis of the PRC2-dependent glial-to-mesenchymal transition happening in the early stages of MPNSTs. We show that PRC2 loss triggers the epigenetic silencing of *SOX10* expression through the closing of chromatin accessibility, contrarily to what happens to *SOX9* that maintains an open chromatin state. *SOX10* is a gliogenesis master regulator transcription factor.[50,51] This supports previous findings in MPNSTs were *SOX10* was found downregulated and epigenetically silenced when compared to benign tumors, and downregulated after PRC2 inactivation in MPNST cell lines.[24,26,49,52] We understand that *SOX10* silencing is key in the loss of SC differentiation capacity by 3KO NCs (Figure 8).

In addition, the absence of PRC2 function triggers the expression of repressed gene programs by the opening of chromatin accessibility. 3KO NC express mesenchymal stem cell genes, maintaining a high expression of SOX9 and other mesenchymal and stemness genes like *TWIST1* and *PRRX1*, in agreement with previous results.[24,25,53] In addition, we identified a consistent upregulation of neurogenesis-associated transcriptional programs in 3KO NC, triggered by PRC2 loss and consistent with previous observations.[2,24,25] The combined analyses of expression and chromatin accessibility, together with the comparison of 2KO with 3KO NCs in one hand, and 3KO NCs with MPNST cell lines (and MSCs) on the other, allowed a mechanistical dissection of these neurogenesis signatures (Figure 8). Some neurogenesis genes (Cluster 1) were immediately expressed after PRC2 inactivation. Some of these genes have been found to be regulated by the REST/NRSF (RE1-silencing transcription factor/Neuron-Restrictive Silencer Factor)-PRC2 complex.[54,55] We hypothesize that in the absence of REST-PRC2-mediated silencing these genes remain accessible and actively transcribed in 3KO cells, including MPNST cell lines. However, other neurogenesis genes (Cluster 3) are accessible to transcription factors upon PRC2 loss, but are only expressed in cells with a clear mesenchymal identity, 3KO MSC and MPNST cells, or even only in MPNST cell lines. This fact underscores that other factors, like those related to cell identity (MSC) or common genomic alterations identified in MPNSTs (copy-number alterations, genome rearrangements) could be potential triggers of these other neurogenesis programs, to reach a genuine mature MPNST state. The analysis of gliogenesis and neurogenesis gene signatures identified in our NC models, in PNF-derived SCs, PNF, ANNUBP, and MPNST tumor samples, confirmed these signatures as part of the glial-to-neuro-mesenchymal transition during benign-to-malignant progression of NF1-related PNS tumors.

Our current model of MPNST development is composed of three stages: 1) early initiating stage characterized by the loss of TSGs; 2) a catastrophic genomic

rearrangement; and 3) if the cell survives, it stabilizes and adopts properties of neuro-mesenchymal NC-like cells (Magallón-Lorenz unpublished data). We have been able to generate histologically compatible MPNST-like tumors by engrafting spheres of 3KO NCs in the sciatic nerve of nude mice (Figure 8). This is the first *in vitro/in vivo* genetically modified MPNST model generated so far, including the inactivation of the three TSGs lost in the natural PNF-ANNUBP-MPNST progression. These cells are deficient in the 3 TSGs but their genome is still 2n. Developed MPNST-like tumors, despite showing high cellularity and a high number of proliferative cells, do not have the aggressive behavior of MPNST PDOX,[56] consistent with an early stage of MPNST development. This 3D model is currently being used for both investigating MPNST progression and for *in vitro* and *in vivo* therapeutic screening (Uriarte-Arrazola unpublished data).

Acknowledgments
We thank the IGTP core facilities and their staff for their contribution and technical support: Translational Genomics Core Facility; Cryobiology, High Performance Computing; Flow Cytometry (Gerard Requena and Marco A. Fernández); IGTP-Hospital Universitari Germans Trias i Pujol (HUGTP) Biobank Facility (Laia Pérez-Roca, Christel Kisser Pioch, Reyes Rodríguez and Lidia Nieto) and Pathology Department (Dr. Pedro Luis González). We thank the Barcelona Stem Cell Bank, Regenerative Medicine Program, IDIBELL, Barcelona, for providing control iPSC line. We also thank the Endocrine Tumor research group led by Dr. Mireia Jordà (IGTP), and particularly Jennifer Marcos and Anna Rueda, for kindly providing lentiviral plasmids and assisting us with the transduction procedures. We are also grateful to the Fundación Proyecto Neurofibromatosis, the Asociación de Afectados de Neurofibromatosis (AANF), and the Catalan Neurofibromatosis Association (ACNefi) for their constant support. This work has mainly been supported by la Fundació La Marató de TV3 (51/C/2019). The work has also been partially supported by the Spanish Ministry of Science and Innovation, Carlos III Health Institute (ISCIII) (PI20/00228, PI23/00422 and PI23/00583) Plan Estatal de I+D+I 2013–2016, co-financed by the FEDER program – a way to build Europe, and by the Government of Catalonia and CERCA Program/Generalitat de Catalunya (2021 SGR 00967). Single cell data generated was supported by Department of Defense office of the Congressionally Directed Medical Research Programs (CDMRP) NFRP FY20 (NF200051). IU-A is supported by a PFIS fellowship from the ISCIII (FI21/00063).

Author contributions
Conceptualization, E.S., M.C., I.U.-A., M.M.-L. and B.G.; methodology, I.U.-A., M.C. and J.F.-R; software and formal analysis, M.M.-L. and B.G.; investigation, I.U.-A., J.F.-R., M.M.-L., B.G., H.M., E.C.-B, J.F.-C., S.O.-B., C.R., M.C. and E.S.; resources, C.L.,E.S.; writing – original draft, I.U.-A., M.C., and E.S.; writing – review & editing, M.M.-L., B.G., I.U.-A, J.F.-C, M.C., and E.S.; visualization, I.U.-A, M.M.-L., B.G., M.C., and E.S.; supervision, B.G., M.C., and E.S.; project administration, M.C. and E.S.; funding acquisition, E.S.

Declaration of interests
The authors declare no competing interests.

Declaration of generative AI and AI-assisted technologies in the writing process
During the preparation of this work, authors used ChatGPT to rephrase or shorten the text. After using this tool, authors reviewed and edited the content as needed and take full responsibility for the content of the publication.

FIGURE LEGENDS

Figure 1. Generation of double knock out *NF*1(-/-) *CDKN2A (-/-)* iPSC lines
(A) Schematic representation of the editing strategy used to knock out the *CDKN2A* locus in *NF1*(-/-) iPSCs, followed by neural crest (NC) formation and Schwann cell (SC) differentiation to generate neurofibromaspheres and assess tumorigenic potential. Sg: sgRNA; Fb: PNF-derived fibroblast.
(B) Left panel: OCT3/4 expression in iPSCs: wild type (WT, *NF1* +/+); 1KO (*NF1* -/-); 2KOp16 (*NF1* -/- *CDKN2A* p16INK4A -/-); and 2KOp14p16 (*NF1* -/- *CDKN2A* -/-). Middle panel: Flow cytometry analysis of p75 and Hnk1 before (iPSC) and after (NC) NC differentiation. Right panel: TFAP2 and SOX10 expression at NC stage. Nuclei counterstained with DAPI. Scale bar: 50 µm.
(C) Left: Micrographs of NC cells after 4 days (d4) of SC differentiation. Scale bar: 100 µm. Right: representative neurofibrompaspheres at day 7 (d7) of SC differentiation, containing also PNF-derived fibroblasts. Scale bar: 100 µm.
(D) Representative immunofluorescence images showing p75 (green) and S100B (red) expression in neurofibromasheres. Nuclei counterstained with DAPI. Scale bar: 100 µm.
(E) Characterization of the tumors grown after engraftment of neurofiromaspheres in the sciatic nerve of nude mice. Left panel: H&E staining. Scale bar: 200 µm. Right panel: Immunofluorescence images for Ku-80 and S100B. Nuclei counterstained with DAPI. Scale bar: 50 µm.
(F) Principal component analysis (PCA) gene expression of WT, 1KO and 2KO cell lines at iPSC and NC stage. One WT in triplicate and three 1KO and 2KO cell lines are shown.
(G) Schematic representation of upregulated genes shared by 2KO NCs and ANNUBPs.
(H) *TYMS* expression in PNFs and ANNUBPs.
(I) Cell viability dose–response curves for pemetrexed treatment after 96h in 1KO_D12 NC, 2KO NC, an *NF1*(+/−) fibroblast cell line, assessed by CellTiter-Glo assay. Mean ± SD of technical replicates (n ≥ 3).
(J) Cell viability after 1.11 µM pemetrexed treatment in cell lines from (I). Mean ± SD of technical replicates (n ≥ 3). Kruskal-Wallis multiple comparison test: *p < 0.05, **p < 0.01.*
(K) Representative micrographs showing density and morphology changes between 1KO_D12 NC and 2KO_A7 NC cell lines and lack of senescence via X-Gal staining (blue) after 96h of 450 nM pemetrexed treatment. Scale bar: 100 µm.

Figure 2. A biological constraint for the inactivation of *NF1*, *CDKN2A* and PRC2 in iPSCs
(A) Schematic representation of the editing strategy used to knock out *SUZ12* in iPSCs and screening workflow for edited clones.
(B) Quantitative analysis of each step in the *SUZ12* editing workflow.

(C) Immunofluorescence detection of H3K27me3 in transfected 1KO and 2KO cell pools. Nuclei counterstained with DAPI. Scale bar: 100 µm.
(D) Immunofluorescence of H3K27me3 in 2KO (p14p16) parental line and an expanded 3KO clone. Nuclei counterstained with DAPI. Scale bar: 100 µm.
(E) Diagram of lentiviral doxycycline-inducible systems for p16 and p14 expression in 2KO and 3KO cell lines.
(F) Schematic representation of the experimental design for inducing p14 and p16 expression in 2KO and 3KO cells. Transduced cells were doxycycline-treated either at 5 (d5) or 8 (d8) days. p16 (mCherry) and p14 (GFP) levels were assessed by flow cytometry. Controls were treated with doxycycline for 24 hours prior to each measured time point (d1, d5 and d8).
(G) Graphical representation of GFP+ and mCherry+ cell populations at 5 (d5) and 8 (d8) days post-doxycycline induction, measured by flow cytometry analysis. Data represent three independent experiments. Unpaired t tests: **, $p < 0.01$; ****, $p < 0.0001$.

Figure 3. Loss of PRC2 function in 2KO iPSCs induces loss of pluripotency and acquisition of a mesenchymal identity
(A) Schematic representation of the acquired cell fate of 2KO cells after *SUZ12* editing in iPSC culture conditions.
(B) Representative micrographs illustrating loss of pluripotency, acquisition of a MSC-like phenotype, and senescence onset in 3KO *SUZ12*-edited cells.
(C) Immunofluorescence images illustrating pluripotency (OCT3/4), PRC2 function (H3K27me3) and mesenchymal identity (SOX9) in 2KO and 3KO cell lines. Nuclei counterstained with DAPI. Scale bar: 50 µm.
(D) Flow cytometry analysis of the MSC markers CD13, CD44 and CD73.
(E) Representative micrographs of senescence analysis (X-Gal staining in blue) in 2KO and 3KO cell lines. Scale bar: 100 µm.

Figure 4. 3KO NC cells capture a glial-to-mesenchymal transition
(A) Schematic representation of the strategy to perpetuate 3KO *SUZ12*-edited cells under NC culture conditions.
(B) Representative micrographs showing NC-like phenotype acquisition of 3KO cells under NC culture conditions. Scale bar: 200 µm.
(C) Flow cytometry analysis for NC markers (p75 and Hnk1) and MSC markers (CD13, CD44 and CD73) in 1KO, 2KO and 3KO cell lines.
(D) Expression of selected NC-glial (*SOX10, NGFR, PLP1*) and NC-mesenchymal (*SOX9, TWIST1, PRRX1*) markers in 2KO (n=3) and 3KO (n=3) cell lines.
(E) t-SNE plots representing single-cell RNA-seq data from nerve, PNF, ANNUBP and MPNST samples. Left panels: representation of cell type composition and sample type distribution. Right panels: Expression of selected NC-glial and NC-mesenchymal markers from (D) in maroon.
(F) Immunofluorescence images of SOX10 and SOX9 expression in 1KO, 2KO and 3KO cell lines. Nuclei counterstained with DAPI. Scale bar: 50 µm.
(G) Heatmap showing the differentially expressed genes of 2KO NC vs 3KO NC cells. See also File S3.

(H) Enrichment analysis of downregulated genes in 3KO cell lines displayed in (G), highlighting gliogenesis-related genes, like *SOX10*.
(I) ATAC-seq chromatin accessibility plot of the *SOX10* locus in 1KO, 2KO and 3KO cell lines, showing epigenetic silencing in 3KO cell lines.
(J) Immunofluorescence images of SOX9, SOX10 and NC-SC markers (p75 and S100B) after 21 days of SC differentiation in 1KO, 2KO and 3KO cell lines. 3KO NCs cannot differentiate into SCs. Nuclei counterstained with DAPI. Scale bar: 50 µm.

Figure 5. **3KO NC spheroids generate human MPNST-like tumors *in vivo* mimicking early-stage MPNST development**
(A) Characterization of tumors arising from 3KO NC spheroid engraftment into the sciatic nerve of nude mice. Upper panel: representative hematoxylin and eosin (H&E) images showing high cellularity and mitotic activity. Scale bar: 200 µm. Lower panel: Ku-80 immunofluorescence with DAPI nuclear counterstaining, showing human origin. Scale bar: 200 µm.
(B) Immunohistochemical comparison of 1KO, 2KO, and 3KO tumor models showing H3K27me3, SOX10, S100B, Vimentin, and Ki-67 expression. Scale bar:100 µm

Figure 6. The MPNST phenotype is markedly affected by PRC2 inactivation and the presence of MSC-like traits.
(A) Schematic overview of the transcriptomic and epigenomic comparison between 3KO NC and MPNSTcl (MPNST cell lines) *in vitro* models.
(B) Schematic representation showing the cell lines used for the omics analyses.
(C) Principal component analysis (PCA) of cell types in (B), comparing transcriptome (i), methylome (ii) and chromatin accessibility (iii). Arrows indicate the impact of genotype on the different cell type identities.
(D) Heatmap showing the expression patterns across all samples of genes differentially expressed between 2KO and 3KO NC. See also File S4.
(E) Enrichment analysis of genes in Cluster 1 from (D). Ellipses represent clusters of related biological processes.
(F) Heatmap showing the differential expression analysis of 3KO NC vs. MPNST cell lines in all samples. See also File S6.
(G) Enrichment analysis of Cluster 3 from (F). Ellipses represent clusters of related biological processes.

Figure 7. Neurogenesis genes: part of MPNST cell identity.
(A) Boxplot showing the expression z-score of Cluster 1 neurogenesis gene signature (Figure 6D).
(B) Volcano-plot showing the differential chromatin accessibility of PRC2 wild-type (1KO, 2KO) vs. PRC2-mutant (3KO) NC cell lines. Neurogenesis genes from Cluster 1 are highlighted in red.
(C) Correlation plot integrating differential gene expression and ATAC-seq data in PRC2 wild-type (1KO, 2KO) vs. PRC2-mutant (3KO) NC cell lines. Neurogenesis genes from Cluster 1 are highlighted in red.
(D) *PITX1* chromatin accessibility plot of 1KO, 2KO, and 3KO NCs and boxplot of *PITX1* normalized expression in all cell lines.

(E) Left panel: *PCSK1* chromatin accessibility plot of 1KO, 2KO, and 3KO NCs and boxplot of *PCSK1* expression in all cell lines. Right panel: t-SNE plot representing single-cell RNA-seq expression of *PCSK1* (maroon) in nerve, PNF, ANNUBP and MPNST samples.
(F) Boxplot showing the normalized expression of Cluster 3 neurogenesis gene signature (Figure 6F).
(G) Volcano-plot showing the differential chromatin accessibility of PRC2 wild-type (1KO, 2KO) vs. PRC2-mutant (3KO) NC cell lines. Neurogenesis genes from Cluster 3 are highlighted in red.
(H) Correlation plot integrating differential gene expression and ATAC-seq data in PRC2-wild-type (1KO, 2KO) and PRC2-mutant (3KO) NC cell lines. Neurogenesis genes from Cluster 3 are highlighted in red.
(I-K) Chromatin accessibility plot of 1KO, 2KO, and 3KO NCs and expression boxplot in all cell lines of *FOXG1* (I), *NR2E1* (J), *DMRT3* (K) Cluster 3 neurogenesis genes.
(L) Correlation plot integrating differential gene expression and ATAC-seq data in PRC2-wild-type (1KO, 2KO) and PRC2-mutant (3KO) NC cell lines. Neurogenesis signature genes from Cluster 1 and 3 highlighted in red; gliogenesis genes from 2KO vs 3KO expression analysis highlighted in blue.
(M) Enrichment analysis of genes with differentially open (top) and closed (bottom) chromatin accessibility regions in PRC2-deficient NC cell lines compared to PRC2-WT NC.
(N) Heatmap showing identified gliogenesis and neurogenesis gene signatures across human NF1-associated PNF-SCs, PNF, ANNUBP, and MPNST samples.

Figure 8. Schematic representation of the generation of the iPSC-derived NC models capturing a glial-to-neuro-mesenchymal transition and malignant progression.
In vitro/in vivo iPSC-derived NC-based model development of the PNF-ANNUBP-MPNST progression. Learned biological insight by model development is highlighted in boxes.

MATERIALS AND METHODS

EXPERIMENTAL MODEL AND SUBJECT DETAILS

Human iPSC lines

The following human induced pluripotent stem cell (hiPSC) lines were utilized in this study: FiPS Ctrl1-SV4F-7 used as a control *NF1*(+/+) cell line and named WT in this article, and *NF1*(-/-) edited FiPS Ctrl1-SV4F-7 previously generated in our lab[36] and named 1KO_D12 in this article. These lines are banked and stored at the Spanish National Stem Cell Bank, Institute of Health Carlos III (BNLC-ISCIII). Their use was approved by the local ethics committee (Clinical Research Ethics Committee of Germans Trias i Pujol Hospital, Badalona, Spain, Project No PI-13-021).
The iPSC lines used were authenticated by PCR-based DNA fingerprinting analysis using the AmpFlSTR_IdentifilerTM PCR Amplification Kit panel from Applied Biosystems.

hiPSC culture

Human iPSCs were cultured on Growth Factor Reduced Matrigel (Corning) diluted at a 1:20 ratio with mTeSR media (StemCell Technologies), and maintained at 37°C in a 5% CO_2 atmosphere. Passage of cells, when necessary, was performed using Accutase (Thermo Fischer Scientific).

CRISPR/Cas9 gene edition

We generated *NF1*(-/-) *CDKN2A* p14ARF(+/+)p16INK4A(-/-) iPSC lines (referred to as 2KO (p16)) and *NF1*(-/-) *CDKN2A* p14ARF(-/-)p16INK4A(-/-) iPSC lines (referred to as 2KO (p14p16)) through CRISPR/Cas9 gene editing of the *NF1*(-/-) edited FiPS Ctrl1-SV4F-7 (referred to as 1KO cell line) using the ArciTect ribonucleoprotein (RNP) system from StemCell Technologies. We next edited *SUZ12* in the 2KO_F9 iPSC line, generating *NF1*(-/-) *CDKN2A* p14ARF(-/-)p16INK4A(-/-) *SUZ12*(-/-) cells (referred to as 3KO).
Briefly, the sgRNAs targeting exon 2 of the *CDKN2A* gene (GTTGTGCTCAGTACTGACTT for 2KO (p16) and GCCCGCATAGATGCCGCGGA for 2KO (p14P16)), exon 1 (GCCGAAAATGGAGCACGTCC) and exon 10 (CGAAGAGTGAACTGCAACGT) of the *SUZ12* gene were introduced into hiPSCs using TransIT-X2 transfection reagent (Mirus), following manufacturer's instructions. Single-cell clones were generated, amplified, and DNA was extracted for *CDKN2A* and *SUZ12* mutation analysis using DNA Sanger sequencing. For the sequencing of each allele, the Gateway Technology cloning method (Invitrogen) was employed using the pDONR 221 vector. Sequences were analyzed using CLC workbench 8 software (Qiagen).

Animal models

All mouse experiments were conducted in accordance with relevant Spanish national laws (RD 1201-/2005) and international guidelines and regulations (European Union rules 2010/63/UE), about the protection of animals used for experimentation and other scientific purposes. The experimental protocols were approved by the IDIBELL Animal Ethic Experimentation Committee (CEEA-IDIBELL approval No 9111) in Spain. They complied with the International Association for Assessment and Accreditation of Laboratory Animal Care procedures (AAALAC). Six-week-old male and female nude mice (Harlan) were used and maintained under sterile air flow isolator conditions,

artificial light-dark cycle of 12 hours, regulated temperature of 22°C, relative humidity of 55%, and fed with autoclaved standard food and acidified water *ad libitum*.

MPNST cell lines and PNF-derived Schwann cells RNAseq data

In this study, we used the RNA-seq data of five NF1-associated MPNST cell lines[30]: S462 (RRID:CVCL_1Y70), ST88-14 (RRID:CVCL_8916), F90-8 (RRID:CVCL_1B47), sNF96.2 (RRID:CVCL_K281) and NMS-2 (RRID:CVCL_4662). This MPNST cell lines contains the most frequently inactivated tumor suppressor genes (TSGs): *NF1*, *CDKN2A* and PRC2.
In this study, we used the RNA-seq data of 3 PNF-derived Schwann cell lines.[36]

Plexiform neurofibromas (PNFs), ANNUBPS, MPNSTs and nerve samples

NF1 patients diagnosed according to standard diagnostic criteria[57] and control patients kindly provided samples after giving written informed consent, with the approval by the Clinical Research Ethics Committee of Germans Trias i Pujol Hospital, Badalona, Spain. Tumor and nerve specimens were obtained after surgery, placed in DMEM medium (Gibco) containing 10% FBS (Gibco) + 1x GlutaMax (Gibco) + 1x Normocin antibiotic cocktail (InvivoGene) and shipped at room temperature to our laboratory. Samples were cut into 1-mm pieces and cryopreserved in 10% DMSO (Sigma) + 90% FBS (Gibco) until used.

METHOD DETAILS

iPSC differentiation toward neural crest (NC)

Neural crest (NC) differentiation was performed as reported elsewhere.[40]

Neural Crest (NC) differentiation towards Mesenchymal Stem Cells (MSC)

Neural crest cells were plated at a density of $6.5x10^4$ cells per cm^2 in DMEM + 10%FBS + 1X Penicillin/Streptomycin (10000units/ml:10000ug/ml) + 1x Glutamax-I 200mM + 90µm 2-bmercaptoethanol onto noncoated tissue culture plates following previously reported protocols.[58] Cells were passaged every 4-5 days using trypsin-EDTA.

Neural Crest (NC) differentiation towards Schwann cells (SCs)

Schwann cell (SC) differentiation was performed as reported previously.[40]

3D spheroid generation

For 1KO and 2KO hiPSC cell lines, Neurofibromasphere generation was performed following previously reported protocols.[36,37]
For 3KO cell lines, sphere generation was conducted as follows: 1.2×10^6 3KO NC-like cells were seeded into AggreWell™ 800 plates pre-treated with Anti-Adherence Rinsing Solution (STEMCELL Technology) in NC media. 48 hours later, spheroids were collected and engrafted into the sciatic nerve of nude mice.

Engraftment experiments

For 1KO and 2KO cell lines, Neurofibromaspheres were engrafted following previously reported protocols.[36,37]
For 3KO cell lines, spheroids containing approximately 2 million cells were resuspended in 1:2 diluted Growth Factor Reduced Matrigel in a total volume of 70µl

of NC medium and injected into the exposed sciatic nerve of nude mice using a 25 G syringe. We injected 1KO, 2KO_C4 and 2KO_F9 cell lines and the three 3KO cell lines (3KO_C6, 3KO_H8 and 3KO_D8). Tumor growth was monitored by manual palpation, and after 4 months, mice were euthanized and tumors fixed in formalin for paraffin embedding.

Immunohistochemical analysis of formalin-fixed paraffin-embedded (FFPE) samples

Hematoxylin & Eosin (H&E) and S100B, SOX10 and Ki67 immunostaining was performed in the IGTP-Germans Trias i Pujol University Hospital (HUGTP) Biobank Facility and Anatomy Pathology Department. Immunohistochemical staining was performed on glass slides after deparaffination and rehydration of formalin-fixed paraffine-embedded tissue. The automatic processing was performed in a Benchmark Ultra (Ventana). Briefly, rehydrated slides were subjected to heat antigen retrieval in CC1 buffer, incubated with primary antibodies and developed with the Ultraview DAB detection system (Ventana).

For H3K27me and vimentin immunostaining endogenous peroxidases were blocked with hydrogen peroxide (H_2O_2 3% for 20 min), and antigen retrieval was performed by heating tissue sections for 20 min in citrate buffer (pH = 6). Blocking was performed with 10% goat serum for 20 min and primary antibodies, vimentin (1:200) and H3K27me3 (1:200) were incubated overnight at 4 °C. The secondary HPRT-conjugated antibody (EnVision; DAKO) was incubated at RT for 30 min. Finally, staining was conducted using diaminobenzidine (DAB; DAKO) for 10 min; nuclei were counterstained with hematoxylin. Images were taken using a Nikon Eclipse 80i vertical microscope. See Table S1 for antibody details.

Fluorescent immunohistochemistry of FFPE samples

FFPE Sections were rehydrated using standard procedures, and antigen retrieval was performed by heating tissue sections for 20 min in citrate buffer (pH = 6). Samples were permeabilized in 0.3% Triton-X in PBS for 30 min, blocked in 1% bovine serum albumin, 10% goat serum (Gibco), 0.1% Triton-X in PBS for 1 hour, and incubated with primary antibodies (S100B, Ku80) diluted in incubation buffer (1% bovine serum albumin with 10% goat serum in PBS and 0.3% TritonX100) overnight at 4ºC. Then, slides were washed 3 times for 10 minutes each in PBS, incubated with secondary antibodies (Alexa Fluor 488 goat anti-mouse, and Alexa Fluor goat 568 anti-rabbit, 1:1000 each) diluted in incubation buffer for 45 minutes, washed again and incubated with DAPI (Stem Cell Technologies, 1:1000) diluted in PBS for 10 minutes. Sections were mounted with Vectashield (Vector laboratories) and secured with polish nail. Images were captured using the DMI 6000B microscope (Leica) and LAS X software (Leica). See Table S1 for antibody details.

DNA extraction

Genomic DNA from cells was extracted using Promega Maxwell 16 system following the manufacturer's instructions (Promega).

RNA extraction

Total RNA from cells was extracted using the 16 LEV simplyRNA Purification Kit (Promega) following manufacturer's instructions in the Maxwell 16 Instrument

(Promega). RNA was quantified with a Nanodrop 1000 spectrophotometer (Thermo Scientific).

Western Blot

Cells were washed twice with chilled PBS and lysed with RIPA buffer (50 mM Tris-HCl (pH 7.4), 150 mM NaCl (Merck), 1mM EDTA (Sigma), 0.5% Igepal CA-630 (Sigma)) supplemented with 3mM DTT (Thermo Fisher), 1mM PMSF (Sigma), 1mM sodium orthovanadate (Sigma), 5mM NaF (Sigma), 10 µg/ml leupeptin (Sigma), 5µg/ml aprotinin (Sigma) and 1xPhosSTOP (Roche). Lysates were quantified using the Pierce BCA Protein Assay Kit (Thermo Fisher Scientific). Lysates were boiled with 1X Laemmli buffer (50% glycerol (v/v) (Sigma), 10% SDS (m/v) (Merck) , 0.05% bromophenol blue (m/v) (Sigma), 25% Tris HCl 1M pH 6.8 (v/v) (Millipore), 5% beta-mercaptoethanol (v/v) (Sigma) in distilled water) and 90 µg of protein was subjected to SDS-PAGE and transferred onto PVDF membranes (18 hours 90 mA at 4°C, for neurofibromin) (1 hours 350 mA at 4°C, for p16INK4A). Membranes were blocked with Odyssey Blocking Buffer (TBS, LI-COR) and incubated with primary antibodies at 4°C overnight; and with mouse anti-αtubulin (Sigma) 1 hour at room temperature. Membranes were then incubated with IRDye 680RD anti-Rabbit and IRDye 800CW anti-Mouse secondary antibodies (1:10,000 each, LI-COR) for 1 hour at room temperature and scanned with the Odyssey CLx (LI-COR) using the Image Studio Lite (LI-COR). See Table S1 for antibody details.

Flow cytometry

Cells were dissociated with accutase and resuspended in 0.1% BSA in PBS. For NC linage markers, cells were incubated for 30 min on ice with unconjugated p75 primary antibody and detected with Alexa Fluor 568-conjugated secondary antibodies, following incubation for 30 min on ice with unconjugated primary antibody Hnk1 and detected with Alexa Fluor 488-conjugated secondary antibodies. For MSC markers, cells were incubated with conjugated APC-CD73, PE-CD13 and PE-CD44 for 15min. Cells were analyzed by flow cytometry using BD FASCCanto II and analyzed using BD FACSDiva 6.2 software. See Table S1 for antibody details.

Immunocytochemical analysis

Cells were fixed in 4% paraformaldehyde (PFA) (Chem Cruz) in PBS for 15 minutes, permeabilized with 0.1%Triton-X100 in PBS for 10 minutes, blocked in 10% FBS in PBS for 15 minutes, and incubated with primary antibodies (OCT3/4, TFAP2, SOX10, SOX9, S100B, p75 and H3K27me3) overnight at 4°C. Secondary antibodies were Alexa Fluor 488 and Alexa Fluor 568 (Thermo Fisher Scientific). Nuclei were stained with DAPI (Stem Cell Technologies, 1:1000). Slides were mounted with Vectashield (Vector laboratories), and coverslips were secured with a polish nail. See Table S1 for antibody details.

Spheroids were fixed in 4% PFA (Chem Cruz) in PBS for 30 minutes at room temperature. The staining protocol was the same as for cells.

Fluorescent and phase contrast images from cells and spheroids were captured using the DMI 6000B microscope (Leica) and LAS X software (Leica).

Senescence assay

Cells were cultured until they reached 70% confluency and senescent cells were stained using the Senescence detection kit (Sigma CS0030) following manufacturer's instructions. Phase contrast images were captured using the DMI 6000B microscope (Leica) and LAS X software (Leica).

Ploidy assay

Five hundred thousand NC cells were seeded on matrigel-coated 6-well plates. After 48h 1 million cells were fixed with 70% cold ethanol overnight at -20°C. Cells were incubated 30min at 37°C with 50µg/ml propidium iodide in PBS-FBS 1% with 100µg/ml RNase and analyzed by flow cytometry using BD FASCCanto II and BD FACSDiva 6.2 software.

Proliferation assay

One hundred fifty thousand NC cells were seeded on matrigel-coated 12-well plates. After 48h cells were treated with 20µM EdU for 1 hour, fixed, permeabilized, and click labeled with Alexa Fluor 488 using Click-iT Plus EdU Flow Cytometry Assay Kits (Thermo Fisher) according to the manufacturer instructions. Cells were also stained with propidium iodide to detect DNA content. Data was collected and analyzed using BD FASCCanto II and BD FACSDiva 6.2 software.

Lentiviral vectors

We generated a Tet Inducible Gene Expression Systems to re-introduce the expression of p14 and p16. We first introduced the helper lentiviral vector pLV-EF1A>Tet3G(ns):T2A:Neo (VB230505-1096yze); and then the inducible lentiviral vectors coding for either p16 (pLV-TRE3G>hCDKN2A[NM_000077.5]:IRES:mCherry-hPGK>Puro (VB230505-1095kwb)) or p14 (pLV-TRE3G>hCDKN2A[NM_058195.4]:IRES:EGFP-hPGK>Hygro (VB230505-1076bgt)). These three vectors were purchased from VectorBuilder.

Viral production and viral transduction

Lentiviral production was performed upon transfection of HEK293T cells using CaCl2 transfection reagent. Packaging vectors used were psPAX2 (Addgene, 12260) and the envelope expression plasmid pCMV-VSV-G (Addgene, #8454). Briefly, 1.4 million of HEK293T cells were seeded in 100mm plates in DMEM 10 %FBS media. 24h later media was changed to NC media and cells were co-transfected with lentiviral vectors. 72h post-transfection, viral supernatant was collected and filtered through a 0.45 µm filter.
Lentiviral transduction was performed in a medium containing viral particles adding 10 mg/mL polybrene for 6 hours. 48h post-transduction cells were selected with antibiotics: G418 (150 µg/mL), Puromycin (0.2-0.4 µg/mL), and Hygromycin (50 µg/mL)
For enrichment of transduced cells, we FACS sorted GFP+ or mCherry+ cells after Doxycycline induction (1 µg/mL) for 24 hours in the Invitrogen *Bigfoot* Spectral Cell *Sorter*. Sorted cells were seeded in NC medium without doxycycline.
For induction experiments, 250.000 cells/well in 12 well plates were seeded and the next day doxycycline (1µg/mL) was added to induce expression of p14 and p16. GFP and mCherry expression were analyzed at 24 hours, 5 days, and 8 days post-induction by flow cytometry using BD LSR Fortessa SORP and BD FACSDiva 6.2 software.

Pemetrexed treatment

1KO and 2KO NC cell lines (1,750 cells/well) and GM00662 *NF1*(+/−) control fibroblasts (750 cells/well) were seeded into 384-well plates (Greiner 781091). 24 hours later, Pemetrexed (LY231514; MedChemExpress) was added in triplicate at seven concentrations using a 1:3 serial dilution starting from 30 µM. After 96 hours of treatment, cell viability was measured using the CellTiter-Glo Luminescent Cell Viability Assay (Promega), and luminescence was quantified with a GloMax Explorer plate reader (Promega). For morphological and senescence assessment, 1KO and 2KO NC cells (15,000 cells/well) were seeded onto chamber slides and incubated overnight. Cells were treated with 450 nM Pemetrexed for 96 hours, and then senescence was evaluated using the Senescence Detection Kit (Sigma-Aldrich, CS0030) according to the manufacturer's protocol. Phase-contrast images were captured using a DMI 6000B microscope (Leica) and LAS X imaging software (Leica).

RNA-seq and analysis

RNAseq library was prepared at BGI (Shenzhen, China) using DNBseq standard protocols. Data was aligned with Salmon v1.8.0 (RRID:SCR_017036)[59] against the UCSC refMrna and hg38 genome. Transcript-level estimates were imported into R (R v4.3.0 Bioconductor v3.17) and summarized to the gene level using tximport (RRID:SCR_016752).[60] Genes with less than 5 counts in more than 2 samples were filtered out. A Principal Component Analysis (PCA) plot was generated. Differentially expressed genes (DEG) between the different cell types were identified using DESeq2 (RRID:SCR_015687)[61] with the Wald test and apglm (RRID:SCR_015687).[62] Genes with an adjusted p-value < 0.05 were considered differentially expressed. Heatmaps were created using the pheatmap package. Finally, we used the clusterProfiler R package (DOI: 10.18129/B9.bioc.clusterProfiler) for DEG enrichment analysis.

DNA methylation

DNA methylation was produced at Diagenode. In short, DNA profiles were generated using the Infinium MethylationEPIC (850k) BeadChip array (Illumina, San Diego, USA) according to the manufacturer's instructions. The data was processed, normalized and filtered using minfi Bioconductor package.[63] We then represent the distribution of the samples according its processed beta values using a PCA.

WGS

The WGS was produced at BGI (Shenzhen, China). In short, the libraries were prepared following standard DNBseq protocols, sequenced in a BGISEQ-500 to a median of 881 million 150-bp paired-end reads per sample, and mapped with BWA-MEM[64] against the GRCh38 genome. WGS data was processed as described elsewhere.[30] In summary, small nucleotide variants were called with Strelka2 and annotated with annovar.[65,66] We called copy-number variation (CNV) using CNVkit[67] with the recommended settings for WGS. As recommended by CNVkit developers, we created a panel of normals and we compared our samples with it. To obtain the exact copy number profile of each sample we used the threshold method, and we provided the Strelka2 germline results for the detection of loss of heterozygosity (LOH) regions. To adjust the thresholds, we calculated the purity of the samples considering the 2n calling and a pseudo-B Allele Frequency (BAF) obtained from the Strelka2 germline results using the

loadSNPDataFromVCF function from CopyNumberPlots R package (10.18129/B9.bioc.CopyNumberPlots). The purity calculation was performed using an in-house function that also considers copy-neutral LOH regions or heterozygous loss regions and pseudo-BAF output. Once the purity was calculated, we estimated the ploidy and manually selected the most accurate CNV calling for each sample. Copy number profiles were plotted using the CopyNumberPlots (10.18129/B9.bioc.CopyNumberPlots) and karyoploteR R packages.[68]

Single-cell RNA-Seq and analysis

scRNA-seq analysis was performed at CNAG in Barcelona. Cryopreserved samples (4 nerves, 4 PNFs, 4 ANNUBPS and 4 MPNSTs) were thawed and digested with 160 U/mL Collagenase Type 1 (Worthington,Lakewood, NJ) and 0.8 U/mL Dispase (Worthington, Lakewood, NJ) for 16 hours at 37ºC 5%CO2. For PNFs, ANNUBPS and MPNSTs the Dead Cell Removal MicroBeads kit (Miltenyi Biotec) was used to eliminate dead cells. For nerve samples the Myelin Removal kit (Milteny Biotec) was used to eliminate myelin and all procedure from this point was conducted at 4ºC. Cells were then resuspended in DMEM + 10% FBS (Gibco) + 1x GlutaMAX (Gibco), filtered with a 40 mm filter and cell viability was calculated with the TC20TM Automated Cell Counter (Bio-Rad). Multiome (scRNA-seq + scATAC-seq) libraries were built following standard protocols and sequenced using an Illumina platform. FASTQ files were processed with cellranger-arc version 2.0.1 (10X Genomics) using the 2020-A-2.0.0 reference based on GRCh38 and Ensembl genes and multiple samples were combined using the cellranger-arc aggr command with the option "–normalize=depth". Merged UMIs per gene per cell matrix was then loaded into R. We performed quality check, filtering (low library size, high mitochondrial content, low number of features) and normalization using scater.[69] We removed highly stressed cells from one sample (scYoga) and doublets (scDblFinder).[70] Data was batch corrected with fastMNN from package batchelor.[71] Cell types were assigned with SingleR[73] based on the HumanPrimaryCellAtlas reference.[72,73] For the graphical representation we performed a dimensionality reduction step with PCA and T-distributed Stochastic Neighbor Embedding (TSNE).

ATACseq

ATACseq was produced at Diagenode. In brief, ATAC-seq reads were mapped to the GRCh38 human reference genome using BWA-MEM[64] and deduplicated Picard MarkDuplicates. We then called peaks with macs2[74] with standard parameters and used deeptools bamCoverage to generate bigwig files for plotting. For differential accessibility, we called consensus peaks with macs2, converted the narrowPeak files into SAF with awk and used featureCounts[75] to create a counts table. Consensus peak counts were imported into R. edgeR[76] was used for normalization and differential analysis between genotypes (1KO and 2KO vs 3KO). Peaks were assigned to genes and a score was calculated for each peak based on p value, log FC and logCPM. The peak with the greatest score was selected to represent each gene in volcano plots and in plots correlating accessibility and expression. Functional enrichment was performed on GO terms with clusterProfiler[77] with genes with a p value below 0.05 and a log fold change over +/- 1 independently for differentially closed and differentially open genes.

Data Visualization

ATAC-seq coverage plots were created from bigwig files with karyoploteR.[68] Heatmaps were plotted with ComplexHeatmap.[78] Boxplots of neurogenesis genes were plotted using R after standardizing the expression data to mean=0 and sd=1. Schemes and diagrams were created with Biorender. Low throughput molecular data was analyzed and plotted with GraphPad Prism (version 7.00).

Supplemental information index

Document S1. Figure S1-S5 and Table S1

File S1. Excel file containing the list of mutations in gene-edited cell lines. Related to Figure 1 and 4.

File S2. Excel file containing the list of genes in common between differentially overexpressed genes in 2KO (n=3) vs 1KO (n=3) and differentially expressed genes in ANNUBPs (n=3) vs. PNFs (n=3). Related to Figure 1.

File S3. Excel file containing the list of differentially expressed genes and enrichment of biological processes between 2KO and 3KO NC cell lines. Related to Figure 4.

File S4. Excel file containing the list of differentially expressed genes and enrichment of biological processes between 3KO and 2KO NC cell lines. Related to Figure 6.

File S5. Excel file containing the list of differentially expressed genes and enrichment of biological processes between 3KO NC and MPNST cell lines. Related to Figure 6.

File S6. Excel file containing the list of differentially open/closed genes and enrichment of biological processes between wild-type PRC2 and mutated PRC2 NC cell lines. Related to Figure 7.

References

1. Lafemina, J., Qin, L.X., Moraco, N.H., Antonescu, C.R., Fields, R.C., Crago, A.M., Brennan, M.F., and Singer, S. (2012). Oncologic outcomes of sporadic, neurofibromatosis-associated, and radiation-induced malignant peripheral nerve sheath tumors. Ann Surg Oncol *20*, 66. https://doi.org/10.1245/S10434-012-2573-2.
2. Lee, W., Teckie, S., Wiesner, T., Ran, L., Prieto Granada, C.N., Lin, M., Zhu, S., Cao, Z., Liang, Y., Sboner, A., et al. (2014). PRC2 is recurrently inactivated through EED or SUZ12 loss in malignant peripheral nerve sheath tumors. Nat Genet *46*, 1227–1232. https://doi.org/10.1038/ng.3095.
3. Grobmyer, S.R., Reith, J.D., Shahlaee, A., Bush, C.H., and Hochwald, S.N. (2008). Malignant peripheral nerve sheath tumor: Molecular pathogenesis and current management considerations. J Surg Oncol *97*, 340–349. https://doi.org/10.1002/JSO.20971.
4. Evans, D.G.R., Baser, M.E., McGaughran, J., Sharif, S., Howard, E., and Moran, A. (2002). Malignant peripheral nerve sheath tumours in neurofibromatosis. J Med Genet *39*, 311–314. https://doi.org/10.1136/jmg.39.5.311.
5. Carli, M., Ferrari, A., Mattke, A., Zanetti, I., Casanova, M., Bisogno, G., Cecchetto, G., Alaggio, R., De Sio, L., Koscielniak, E., et al. (2005). Pediatric malignant peripheral nerve sheath tumor: The Italian and German Soft Tissue Sarcoma Cooperative Group. Journal of Clinical Oncology *23*, 8422–8430. https://doi.org/10.1200/JCO.2005.01.4886.
6. Uusitalo, E., Rantanen, M., Kallionpää, R.A., Pöyhönen, M., Leppävirta, J., Ylä-Outinen, H., Riccardi, V.M., Pukkala, E., Pitkäniemi, J., Peltonen, S., et al. (2016). Distinctive Cancer Associations in Patients With Neurofibromatosis Type 1. Journal of Clinical Oncology *34*, 1978–1986. https://doi.org/10.1200/JCO.2015.65.3576.
7. Ferner, R.E., and Gutmann, D.H. (2002). International Consensus Statement on Malignant Peripheral Nerve Sheath Tumors in Neurofibromatosis 1 1. Cancer Res *62*, 1573–1577.
8. Prada, C.E., Rangwala, F.A., Martin, L.J., Lovell, A.M., Saal, H.M., Schorry, E.K., and Hopkin, R.J. (2012). Pediatric plexiform neurofibromas: Impact on morbidity and mortality in neurofibromatosis type 1. Journal of Pediatrics *160*, 461–467. https://doi.org/10.1016/j.jpeds.2011.08.051.
9. Le Guellec, S., Decouvelaere, A.V., Filleron, T., Valo, I., Charon-Barra, C., Robin, Y.M., Terrier, P., Chevreau, C., and Coindre, J.M. (2016). Malignant peripheral nerve sheath tumor is a challenging diagnosis. American Journal of Surgical Pathology *40*, 896–908. https://doi.org/10.1097/PAS.0000000000000655.
10. Anghileri, M., Miceli, R., Fiore, M., Mariani, L., Ferrari, A., Mussi, C., Lozza, L., Collini, P., Olmi, P., Casali, P.G., et al. (2006). Malignant peripheral nerve sheath tumors: Prognostic factors and survival in a series of patients treated at a single institution. Cancer *107*, 1065–1074. https://doi.org/10.1002/CNCR.22098.
11. Porter, D.E., Prasad, V., Foster, L., Dall, G.F., Birch, R., and Grimer, R.J. (2009). Survival in Malignant Peripheral Nerve Sheath Tumours: A Comparison between Sporadic and Neurofibromatosis Type 1-Associated Tumours. Sarcoma *2009*, 756395. https://doi.org/10.1155/2009/756395.

12. Moretti, V.M., Crawford, E.A., Staddon, A.P., Lackman, R.D., and Ogilvie, C.M. (2011). Early outcomes for malignant peripheral nerve sheath tumor treated with chemotherapy. American Journal of Clinical Oncology: Cancer Clinical Trials *34*, 417–421. https://doi.org/10.1097/COC.0B013E3181E9C08A.
13. Kourea, H.P., Orlow, I., Scheithauer, B.W., Cordon-Cardo, C., and Woodruff, J.M. (1999). Deletions of the INK4A Gene Occur in Malignant Peripheral Nerve Sheath Tumors but not in Neurofibromas. https://doi.org/10.1016/S0002-9440(10)65504-6.
14. Nielsen, G.P., Stemmer-Rachamimov, A.O., Ino, Y., Møller, M.B., Rosenberg, A.E., and Louis, D.N. (1999). Malignant transformation of neurofibromas in neurofibromatosis 1 is associated with CDKN2A/p16 inactivation. American Journal of Pathology *155*, 1879–1884. https://doi.org/10.1016/S0002-9440(10)65507-1.
15. Beert, E., Brems, H., Daniëls, B., de Wever, I., van Calenbergh, F., Schoenaers, J., Debiec-Rychter, M., Gevaert, O., de Raedt, T., van den Bruel, A., et al. (2011). Atypical neurofibromas in neurofibromatosis type 1 are premalignant tumors. Genes Chromosomes Cancer *50*, 1021–1032. https://doi.org/10.1002/GCC.20921.
16. Miettinen, M.M., Antonescu, C.R., Fletcher, C.D.M., Kim, A., Lazar, A.J., Quezado, M.M., Reilly, K.M., Stemmer-Rachamimov, A., Stewart, D.R., Viskochil, D., et al. (2017). Histopathologic evaluation of atypical neurofibromatous tumors and their transformation into malignant peripheral nerve sheath tumor in patients with neurofibromatosis 1—a consensus overview. Hum Pathol *67*, 1–10. https://doi.org/10.1016/J.HUMPATH.2017.05.010.
17. Higham, C.S., Dombi, E., Rogiers, A., Bhaumik, S., Pans, S., Connor, S.E.J., Miettinen, M., Sciot, R., Tirabosco, R., Brems, H., et al. (2018). The characteristics of 76 atypical neurofibromas as precursors to neurofibromatosis 1 associated malignant peripheral nerve sheath tumors. Neuro Oncol *20*, 818–825. https://doi.org/10.1093/NEUONC/NOY013.
18. Carrió, M., Gel, B., Terribas, E., Zucchiatti, A.C., Moliné, T., Rosas, I., Teulé, Á., Ramón y Cajal, S., López-Gutiérrez, J.C., Blanco, I., et al. (2018). Analysis of intratumor heterogeneity in Neurofibromatosis type 1 plexiform neurofibromas and neurofibromas with atypical features: Correlating histological and genomic findings. Hum Mutat *39*, 1112–1125. https://doi.org/10.1002/HUMU.23552.
19. Pemov, A., Hansen, N.F., Sindiri, S., Patidar, R., Higham, C.S., Dombi, E., Miettinen, M.M., Fetsch, P., Brems, H., Chandrasekharappa, S.C., et al. (2019). Low mutation burden and frequent loss of CDKN2A/B and SMARCA2, but not PRC2, define premalignant neurofibromatosis type 1-associated atypical neurofibromas. Neuro Oncol *21*, 981–992. https://doi.org/10.1093/NEUONC/NOZ028.
20. Cortes-Ciriano, I., Steele, C.D., Piculell, K., Al-Ibraheemi, A., Eulo, V., Bui, M.M., Chatzipli, A., Dickson, B.C., Borcherding, D.C., Feber, A., et al. (2023). Genomic Patterns of Malignant Peripheral Nerve Sheath Tumor (MPNST) Evolution Correlate with Clinical Outcome and Are Detectable in Cell-Free DNA. Cancer Discov *13*, 654. https://doi.org/10.1158/2159-8290.CD-22-0786.
21. Buchstaller, J., Clapp, D.W., Parada, L.F., and Zhu, Y. (2012). Cell of Origin and the Contribution of Microenvironment in NF1 Tumorigenesis and Therapeutic

Implications. In: Upadhyaya, M., Cooper, D. (eds) Neurofibromatosis Type 1. (Springer, Berlin, Heidelberg) https://doi.org/10.1007/978-3-642-32864-0_36.
22. Comet, I., Riising, E.M., Leblanc, B., and Helin, K. (2016). Maintaining cell identity: PRC2-mediated regulation of transcription and cancer. Nature Reviews Cancer 2016 16:12 *16*, 803–810. https://doi.org/10.1038/nrc.2016.83.
23. De Raedt, T., Beert, E., Pasmant, E., Luscan, A., Brems, H., Ortonne, N., Helin, K., Hornick, J.L., Mautner, V., Kehrer-Sawatzki, H., et al. (2014). PRC2 loss amplifies Ras-driven transcription and confers sensitivity to BRD4-based therapies. Nature 2014 514:7521 *514*, 247–251. https://doi.org/10.1038/nature13561.
24. Kochat, V., Raman, A.T., Landers, S.M., Tang, M., Schulz, J., Terranova, C., Landry, J.P., Bhalla, A.D., Beird, H.C., Wu, C.C., et al. (2021). Enhancer reprogramming in PRC2-deficient malignant peripheral nerve sheath tumors induces a targetable de-differentiated state. Acta Neuropathol *142*, 565–590. https://doi.org/10.1007/S00401-021-02341-Z.
25. Zhang, X., Lou, H.E., Gopalan, V., Kelly, M.C., Hannenhalli, S., Shern Correspondence, J.F., Liu, Z., Jafarah, H.M., Lei, H., Jones, P., et al. (2022). Single-cell sequencing reveals activation of core transcription factors in PRC2-deficient malignant peripheral nerve sheath tumor. Cell Rep *40*, 111363. https://doi.org/10.1016/j.celrep.2022.111363.
26. Vasudevan, H.N., Payne, E., Delley, C.L., John Liu, S., Mirchia, K., Sale, M.J., Lastella, S., Nunez, M.S., Lucas, C.H.G., Eaton, C.D., et al. (2024). Functional interactions between neurofibromatosis tumor suppressors underlie Schwann cell tumor de-differentiation and treatment resistance. Nat Commun *15*, 477. https://doi.org/10.1038/S41467-024-44755-9.
27. Verdijk, R.M., Den Bakker, M.A., Dubbink, H.J., Hop, W.C.J., Dinjens, W.N.M., and Kros, J.M. (2010). TP53 Mutation Analysis of Malignant Peripheral Nerve Sheath Tumors. J Neuropathol Exp Neurol *69*, 16–26. https://doi.org/10.1097/NEN.0B013E3181C55D55.
28. Høland, M., Kolberg, M., Danielsen, S.A., Bjerkehagen, B., Eilertsen, I.A., Hektoen, M., Mandahl, N., van den Berg, E., Smeland, S., Mertens, F., et al. (2018). Inferior survival for patients with malignant peripheral nerve sheath tumors defined by aberrant TP53. Modern Pathology *31*, 1694–1707. https://doi.org/10.1038/S41379-018-0074-Y.
29. Abeshouse, A., Adebamowo, C., Adebamowo, S.N., Akbani, R., Akeredolu, T., Ally, A., Anderson, M.L., Anur, P., Appelbaum, E.L., Armenia, J., et al. (2017). Comprehensive and Integrated Genomic Characterization of Adult Soft Tissue Sarcomas. Cell *171*, 950-965.e28. https://doi.org/10.1016/J.CELL.2017.10.014.
30. Magallón-Lorenz, M., Terribas, E., Ortega-Bertran, S., Creus-Bachiller, E., Fernández, M., Requena, G., Rosas, I., Mazuelas, H., Uriarte-Arrazola, I., Negro, A., et al. (2023). Deep genomic analysis of malignant peripheral nerve sheath tumor cell lines challenges current malignant peripheral nerve sheath tumor diagnosis. iScience *26*. https://doi.org/10.1016/j.isci.2023.106096.
31. Serra, E., Gel, B., Fernández-Rodríguez, J., and Lázaro, C. (2020). Genomics of Peripheral Nerve Sheath Tumors Associated with Neurofibromatosis Type 1. In: Tadini, G., Legius, E., Brems, H. (eds) Multidisciplinary Approach to Neurofibromatosis Type 1. (Springer, Cham) https://doi.org/10.1007/978-3-319-92450-2_9.

32. Somatilaka, B.N., Sadek, A., McKay, R.M., and Le, L.Q. (2022). Malignant Peripheral Nerve Sheath Tumor: Models, Biology, and Translation. Oncogene *41*, 2405. https://doi.org/10.1038/S41388-022-02290-1.
33. Onfroy, A. (2024). Identification des mécanismes cellulaires et moléculaires gouvernant la transformation maligne dans la Neurofibromatose de Type 1, en assurant la reproductibilité des analyses transcriptomiques (Doctoral dissertation). Université Paris-Est, Créteil. https://theses.fr/s298476.
34. Rhodes, S.D., He, Y., Smith, A., Jiang, L., Lu, Q., Mund, J., Li, X., Bessler, W., Qian, S., Dyer, W., et al. (2019). Cdkn2a (Arf) loss drives NF1-associated atypical neurofibroma and malignant transformation. Hum Mol Genet *28*, 2752–2762. https://doi.org/10.1093/HMG/DDZ095.
35. Chaney, K.E., Perrino, M.R., Kershner, L.J., Patel, A. V., Wu, J., Choi, K., Rizvi, T.A., Dombi, E., Szabo, S., Largaespada, D.A., et al. (2021). Cdkn2a loss in a model of neurofibroma demonstrates stepwise tumor progression to atypical neurofibroma and mpnst. Cancer Res *80*, 4720–4730. https://doi.org/10.1158/0008-5472.CAN-19-1429.
36. Mazuelas, H., Magallón-Lorenz, M., Fernández-Rodríguez, J., Uriarte-Arrazola, I., Richaud-Patin, Y., Terribas, E., Villanueva, A., Castellanos, E., Blanco, I., Raya, Á., et al. (2022). Modeling iPSC-derived human neurofibroma-like tumors in mice uncovers the heterogeneity of Schwann cells within plexiform neurofibromas. Cell Rep *38*. https://doi.org/10.1016/J.CELREP.2022.110385.
37. Mazuelas, H., Uriarte-Arrazola, I., Fernández-Rodríguez, J., Magallón-Lorenz, M., Villanueva, A., Lázaro, C., Gel, B., Serra, E., and Carrió, M. (2023). Generation of human iPSC-derived neurofibromaspheres for in vitro and in vivo uses. STAR Protoc *4*, 102198. https://doi.org/10.1016/J.XPRO.2023.102198.
38. Benfatto, S., Serçin, Ö., Dejure, F.R., Abdollahi, A., Zenke, F.T., and Mardin, B.R. (2021). Uncovering cancer vulnerabilities by machine learning prediction of synthetic lethality. Mol Cancer *20*, 1–22. https://doi.org/10.1186/S12943-021-01405-8.
39. Magallón-Lorenz, M., Fernández-Rodríguez, J., Terribas, E., Creus-Batchiller, E., Romagosa, C., Estival, A., Perez Sidelnikova, D., Salvador, H., Villanueva, A., Blanco, I., et al. (2021). Chromosomal translocations inactivating CDKN2A support a single path for malignant peripheral nerve sheath tumor initiation. Hum Genet *140*, 1241–1252. https://doi.org/10.1007/S00439-021-02296-X.
40. Carrió, M., Mazuelas, H., Richaud-Patin, Y., Gel, B., Terribas, E., Rosas, I., Jimenez-Delgado, S., Biayna, J., Vendredy, L., Blanco, I., et al. (2019). Reprogramming Captures the Genetic and Tumorigenic Properties of Neurofibromatosis Type 1 Plexiform Neurofibromas. Stem Cell Reports *12*, 639. https://doi.org/10.1016/J.STEMCR.2019.02.001.
41. Joseph, N.M., Mosher, J.T., Buchstaller, J., Snider, P., McKeever, P.E., Lim, M., Conway, S.J., Parada, L.F., Zhu, Y., and Morrison, S.J. (2008). The loss of Nf1 transiently promotes self-renewal but not tumorigenesis by neural crest stem cells. Cancer Cell *13*, 129. https://doi.org/10.1016/J.CCR.2008.01.003.
42. López-Cortés, A., Abarca, E., Silva, L., Velastegui, E., León-Sosa, A., Karolys, G., Cabrera, F., and Caicedo, A. (2021). Identification of key proteins in the signaling crossroads between wound healing and cancer hallmark phenotypes. Scientific Reports 2021 11:1 *11*, 1–16. https://doi.org/10.1038/s41598-021-96750-5.

43. Lucas, C.H.G., Gross, A.M., Romo, C.G., Dehner, C.A., Lazar, A.J., Miettinen, M., Pekmezci, M., Quezado, M., Rodriguez, F.J., Stemmer-Rachamimov, A., et al. (2025). Consensus recommendations for an integrated diagnostic approach to peripheral nerve sheath tumors arising in the setting of Neurofibromatosis Type 1. Neuro Oncol *27*, 616–624. https://doi.org/10.1093/NEUONC/NOAE235.
44. Lee, T.I., Jenner, R.G., Boyer, L.A., Guenther, M.G., Levine, S.S., Kumar, R.M., Chevalier, B., Johnstone, S.E., Cole, M.F., Isono, K. ichi, et al. (2006). Control of Developmental Regulators by Polycomb in Human Embryonic Stem Cells. Cell *125*, 301–313. https://doi.org/10.1016/j.cell.2006.02.043.
45. De Raedt, T., Maertens, O., Chmara, M., Brems, H., Heyns, I., Sciot, R., Majounie, E., Upadhyaya, M., De Schepper, S., Speleman, F., et al. (2006). Somatic loss of wild type NF1 allele in neurofibromas: Comparison of NF1 microdeletion and non-microdeletion patients. Genes Chromosomes Cancer *45*, 893–904. https://doi.org/10.1002/GCC.20353.
46. Bracken, A.P., Kleine-Kohlbrecher, D., Dietrich, N., Pasini, D., Gargiulo, G., Beekman, C., Theilgaard-Mönch, K., Minucci, S., Porse, B.T., Marine, J.C., et al. (2007). The Polycomb group proteins bind throughout the INK4A-ARF locus and are disassociated in senescent cells. Genes Dev *21*, 525. https://doi.org/10.1101/GAD.415507.
47. Gomez-Sanchez, J.A., Gomis-Coloma, C., Morenilla-Palao, C., Peiro, G., Serra, E., Serrano, M., and Cabedo, H. (2013). Epigenetic induction of the Ink4a/Arf locus prevents Schwann cell overproliferation during nerve regeneration and after tumorigenic challenge. Brain *136*, 2262–2278. https://doi.org/10.1093/BRAIN/AWT130.
48. Shan, Y., Liang, Z., Xing, Q., Zhang, T., Wang, B., Tian, S., Huang, W., Zhang, Y., Yao, J., Zhu, Y., et al. (2017). PRC2 specifies ectoderm lineages and maintains pluripotency in primed but not naïve ESCs. Nat Commun *8*, 1–14. https://doi.org/10.1038/S41467-017-00668-4.
49. Wu, L.M.N., Zhang, F., Rao, R., Adam, M., Pollard, K., Szabo, S., Liu, X., Belcher, K.A., Luo, Z., Ogurek, S., et al. (2022). Single-cell multiomics identifies clinically relevant mesenchymal stem-like cells and key regulators for MPNST malignancy. Sci Adv *8*, eabo5442. https://doi.org/10.1126/SCIADV.ABO5442.
50. Britsch, S., Goerich, D.E., Riethmacher, D., Peirano, R.I., Rossner, M., Nave, K.A., Birchmeier, C., and Wegner, M. (2001). The transcription factor Sox10 is a key regulator of peripheral glial development. Genes Dev *15*, 66. https://doi.org/10.1101/GAD.186601.
51. Mollaaghababa, R., and Pavan, W.J. (2003). The importance of having your SOX on: Role of SOX10 in the development of neural crest-derived melanocytes and glia. Oncogene *22*, 3024–3034. https://doi.org/10.1038/SJ.ONC.1206442.
52. Miller, S.J., Rangwala, F., Williams, J., Ackerman, P., Kong, S., Jegga, A.G., Kaiser, S., Aronow, B.J., Frahm, S., Kluwe, L., et al. (2006). Large-Scale Molecular Comparison of Human Schwann Cells to Malignant Peripheral Nerve Sheath Tumor Cell Lines and Tissues. Cancer Res *66*, 2584–2591. https://doi.org/10.1158/0008-5472.CAN-05-3330.
53. Miller, S.J., Jessen, W.J., Mehta, J., Hardiman, A., Sites, E., Kaiser, S., Jegga, A.G., Li, H., Upadhyaya, M., Giovannini, M., et al. (2009). Integrative genomic analyses

of neurofibromatosis tumours identify SOX9 as a biomarker and survival gene. EMBO Mol Med *1*, 236–248. https://doi.org/10.1002/EMMM.200900027.

54. Dietrich, N., Lerdrup, M., Landt, E., Agrawal-Singh, S., Bak, M., Tommerup, N., Rappsilber, J., Södersten, E., and Hansen, K. (2012). REST–Mediated Recruitment of Polycomb Repressor Complexes in Mammalian Cells. PLoS Genet *8*, e1002494. https://doi.org/10.1371/JOURNAL.PGEN.1002494.
55. Arnold, P., Schöler, A., Pachkov, M., Balwierz, P.J., Jørgensen, H., Stadler, M.B., Van Nimwegen, E., and Schübeler, D. (2013). Modeling of epigenome dynamics identifies transcription factors that mediate Polycomb targeting. Genome Res *23*, 60–73. https://doi.org/10.1101/GR.142661.112.
56. Ortega-Bertran, S., Fernández-Rodríguez, J., Magallón-Lorenz, M., Zhang, X., Creus-Bachiller, E., Diazgranados, A.P., Uriarte-Arrazola, I., Mazuelas, H., Blanco, I., Valverde, C., et al. (2025). Triple Combination of MEK, BET, and CDK Inhibitors Significantly Reduces Human Malignant Peripheral Nerve Sheath Tumors in Mouse Models. Clinical Cancer Research *31*, 907–920. https://doi.org/10.1158/1078-0432.CCR-24-2807.
57. DeBella, K., Szudek, J., and Friedman, J.M. (2000). Use of the National Institutes of Health Criteria for Diagnosis of Neurofibromatosis 1 in Children. Pediatrics *105*, 608–614. https://doi.org/10.1542/PEDS.105.3.608.
58. Menendez, L., Kulik, M.J., Page, A.T., Park, S.S., Lauderdale, J.D., Cunningham, M.L., and Dalton, S. (2013). Directed differentiation of human pluripotent cells to neural crest stem cells. Nature Protocols 2013 8:1 *8*, 203–212. https://doi.org/10.1038/nprot.2012.156.
59. Patro, R., Duggal, G., Love, M.I., Irizarry, R.A., and Kingsford, C. (2017). Salmon provides fast and bias-aware quantification of transcript expression. Nat Methods *14*, 417–419. https://doi.org/10.1038/NMETH.4197.
60. Soneson, C., Love, M.I., and Robinson, M.D. (2016). Differential analyses for RNA-seq: transcript-level estimates improve gene-level inferences. F1000Res *4*, 1521. https://doi.org/10.12688/F1000RESEARCH.7563.2.
61. Love, M.I., Huber, W., and Anders, S. (2014). Moderated estimation of fold change and dispersion for RNA-seq data with DESeq2. Genome Biol *15*, 1–21. https://doi.org/10.1186/S13059-014-0550-8.
62. Zhu, A., Ibrahim, J.G., and Love, M.I. (2019). Heavy-tailed prior distributions for sequence count data: removing the noise and preserving large differences. Bioinformatics *35*, 2084–2092. https://doi.org/10.1093/BIOINFORMATICS/BTY895.
63. Aryee, M.J., Jaffe, A.E., Corrada-Bravo, H., Ladd-Acosta, C., Feinberg, A.P., Hansen, K.D., and Irizarry, R.A. (2014). Minfi: a flexible and comprehensive Bioconductor package for the analysis of Infinium DNA methylation microarrays. Bioinformatics *30*, 1363–1369. https://doi.org/10.1093/BIOINFORMATICS/BTU049.
64. Li, H. (2013). Aligning sequence reads, clone sequences and assembly contigs with BWA-MEM. https://doi.org/10.48550/arXiv.1303.3997.
65. Kim, S., Scheffler, K., Halpern, A.L., Bekritsky, M.A., Noh, E., Källberg, M., Chen, X., Kim, Y., Beyter, D., Krusche, P., et al. (2018). Strelka2: fast and accurate calling of germline and somatic variants. Nature Methods 2018 15:8 *15*, 591–594. https://doi.org/10.1038/s41592-018-0051-x.

66. Wang, K., Li, M., and Hakonarson, H. (2010). ANNOVAR: functional annotation of genetic variants from high-throughput sequencing data. Nucleic Acids Res *38*, e164–e164. https://doi.org/10.1093/NAR/GKQ603.
67. Talevich, E., Shain, A.H., Botton, T., and Bastian, B.C. (2016). CNVkit: Genome-Wide Copy Number Detection and Visualization from Targeted DNA Sequencing. PLoS Comput Biol *12*, e1004873. https://doi.org/10.1371/JOURNAL.PCBI.1004873.
68. Gel, B., and Serra, E. (2017). karyoploteR: an R/Bioconductor package to plot customizable genomes displaying arbitrary data. Bioinformatics *33*, 3088–3090. https://doi.org/10.1093/BIOINFORMATICS/BTX346.
69. McCarthy, D.J., Campbell, K.R., Lun, A.T.L., and Wills, Q.F. (2017). Scater: pre-processing, quality control, normalization and visualization of single-cell RNA-seq data in R. Bioinformatics *33*, 1179–1186. https://doi.org/10.1093/BIOINFORMATICS/BTW777.
70. Germain, P.L., Robinson, M.D., Lun, A., Garcia Meixide, C., and Macnair, W. (2022). Doublet identification in single-cell sequencing data using scDblFinder. F1000Res *10*, 979. https://doi.org/10.12688/F1000RESEARCH.73600.2.
71. Haghverdi, L., Lun, A.T.L., Morgan, M.D., and Marioni, J.C. (2018). Batch effects in single-cell RNA-sequencing data are corrected by matching mutual nearest neighbors. Nat Biotechnol *36*, 421–427. https://doi.org/10.1038/NBT.4091.
72. Aran, D., Looney, A.P., Liu, L., Wu, E., Fong, V., Hsu, A., Chak, S., Naikawadi, R.P., Wolters, P.J., Abate, A.R., et al. (2019). Reference-based analysis of lung single-cell sequencing reveals a transitional profibrotic macrophage. Nature Immunology 2019 20:2 *20*, 163–172. https://doi.org/10.1038/s41590-018-0276-y.
73. Mabbott, N.A., Baillie, J.K., Brown, H., Freeman, T.C., and Hume, D.A. (2013). An expression atlas of human primary cells: Inference of gene function from coexpression networks. BMC Genomics *14*, 1–13. https://doi.org/10.1186/1471-2164-14-632.
74. Zhang, Y., Liu, T., Meyer, C.A., Eeckhoute, J., Johnson, D.S., Bernstein, B.E., Nussbaum, C., Myers, R.M., Brown, M., Li, W., et al. (2008). Model-based analysis of ChIP-Seq (MACS). Genome Biol *9*, 1–9. https://doi.org/10.1186/GB-2008-9-9-R137.
75. Liao, Y., Smyth, G.K., and Shi, W. (2014). featureCounts: an efficient general purpose program for assigning sequence reads to genomic features. Bioinformatics *30*, 923–930. https://doi.org/10.1093/BIOINFORMATICS/BTT656.
76. Robinson, M.D., McCarthy, D.J., and Smyth, G.K. (2010). edgeR: a Bioconductor package for differential expression analysis of digital gene expression data. Bioinformatics *26*, 139–140. https://doi.org/10.1093/BIOINFORMATICS/BTP616.
77. Yu, G., Wang, L.G., Han, Y., and He, Q.Y. (2012). ClusterProfiler: An R package for comparing biological themes among gene clusters. OMICS *16*, 284–287. https://doi.org/10.1089/OMI.2011.0118.
78. Gu, Z., Eils, R., and Schlesner, M. (2016). Complex heatmaps reveal patterns and correlations in multidimensional genomic data. Bioinformatics *32*, 2847–2849. https://doi.org/10.1093/BIOINFORMATICS/BTW313.

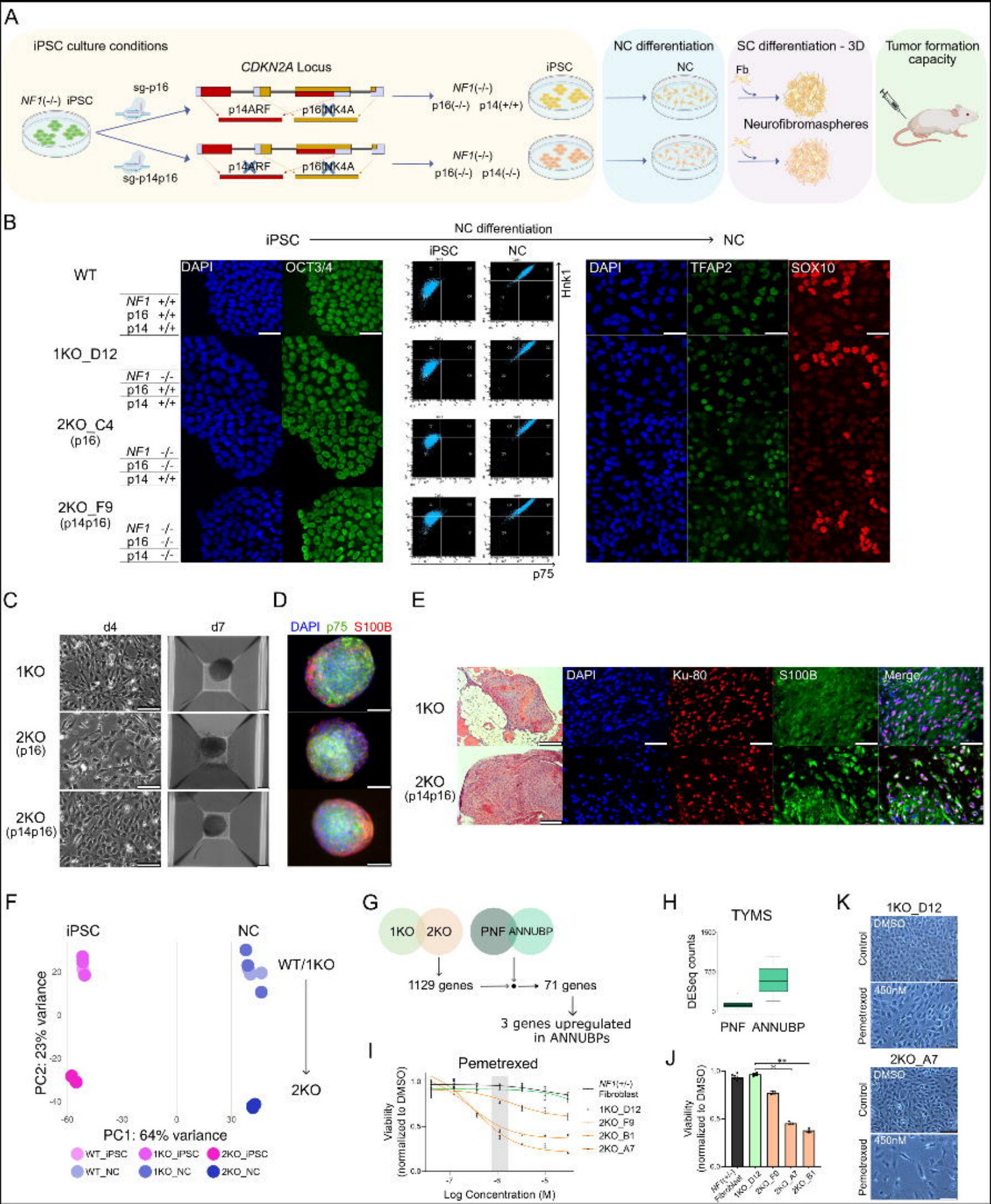
A
iPSC culture conditions
NF1(-/-) iPSC
sg-p16
sg-p14p16
CDKN2A Locus
p14ARF
p16INK4A
NF1(-/-)
p16(-/-) p14(+/+)
p16(-/-) p14(-/-)
iPSC
NC differentiation
NC
SC differentiation - 3D
Fb
Neurofibromaspheres
Tumor formation capacity
B
iPSC
NC differentiation
NC
WT
1KO_D12
2KO_C4 (p16)
2KO_F9 (p14p16)
NF1 +/+
p16 +/+
p14 +/+
NF1 -/-
p16 +/+
p14 +/+
NF1 -/-
p16 -/-
p14 +/+
NF1 -/-
p16 -/-
p14 -/-
DAPI
OCT3/4
Hnk1
p75
TFAP2
SOX10
C
d4
d7
1KO
2KO (p16)
2KO (p14p16)
D
DAPI p75 S100B
E
1KO
2KO (p14p16)
DAPI
Ku-80
S100B
Merge
F
iPSC
NC
WT/1KO
2KO
PC2: 23% variance
PC1: 64% variance
WT_iPSC
1KO_iPSC
2KO_iPSC
WT_NC
1KO_NC
2KO_NC
G
1KO 2KO
PNF ANNUBP
1129 genes
71 genes
3 genes upregulated in ANNUBPs
H
TYMS
DESeq counts
PNF ANNUBP
I
Pemetrexed
Viability (normalized to DMSO)
Log Concentration (M)
NF1(+/-) Fibroblast
1KO_D12
2KO_F9
2KO_B1
2KO_A7
J
Viability (normalized to DMSO)
NF1(+/-) Fibroblast
1KO_D12
2KO_F9
2KO_A7
2KO_B1
K
1KO_D12
2KO_A7
Control
Pemetrexed
DMSO
450nM

A

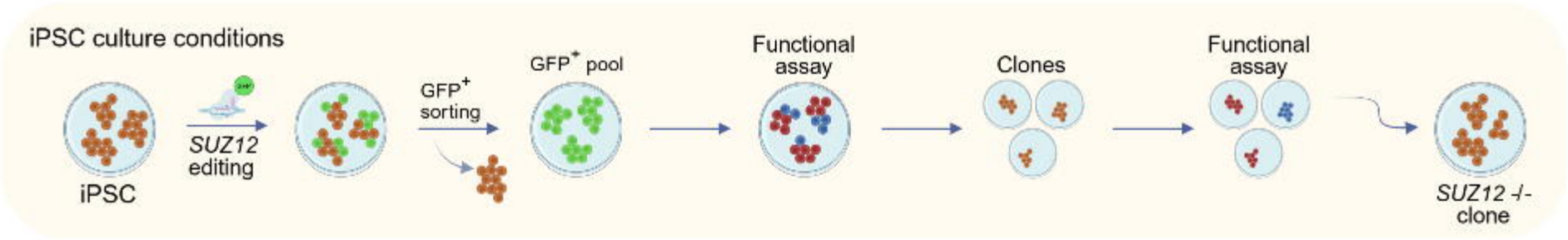

B

Cell lines	Genotype	Transfections	Edited cell pools	Analyzed clones	Edited clones	Expanded clones
1KO	*NF1* (-/-) p14 (+/+) p16 (+/+)	4	2	29	1	0
2KO (p16)	*NF1*(-/-) p14 (+/+) p16 (-/-)	4	4	30	3	0
2KO (p14p16)	*NF1*(-/-) p14 (-/-) p16 (-/-)	5	4	46	8	4

C

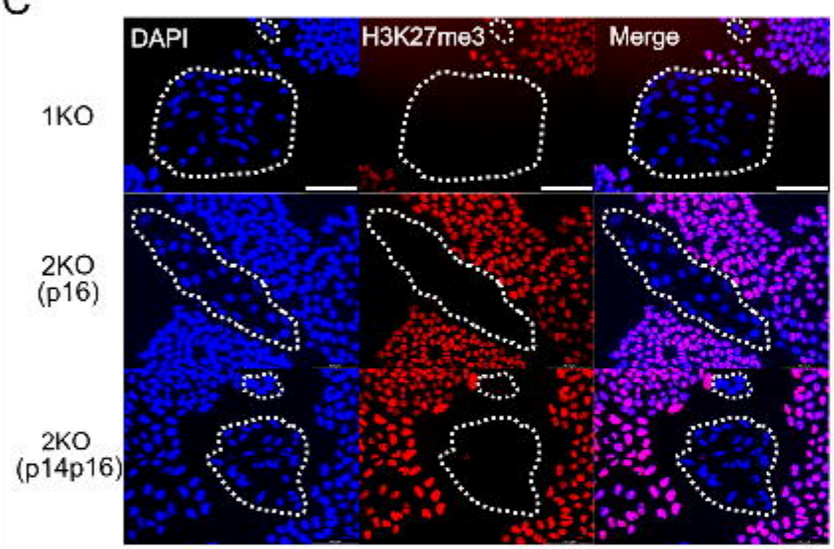

D

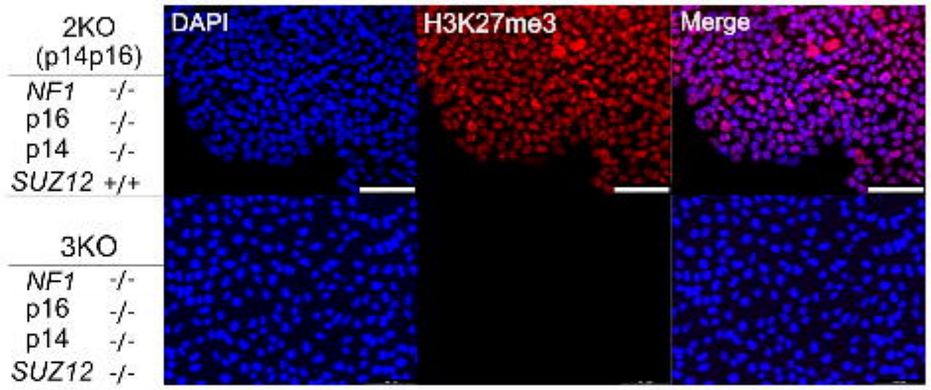

E

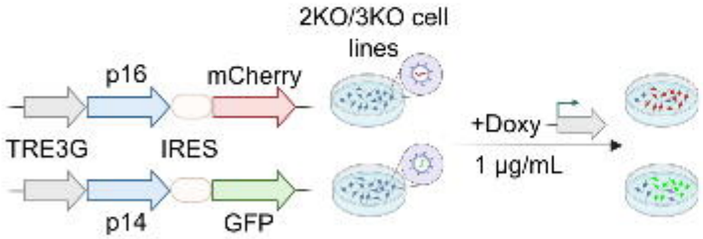

F

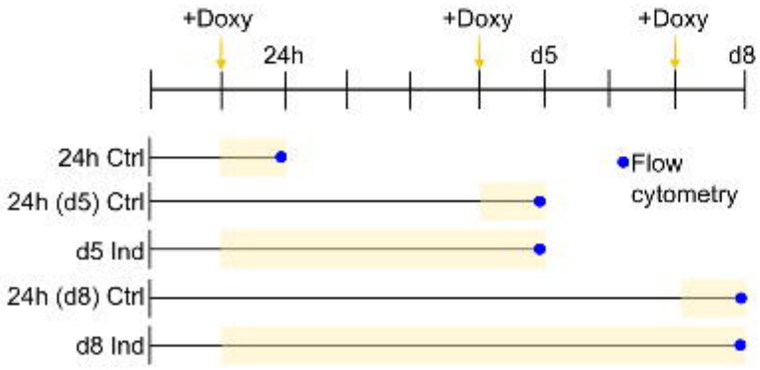

G

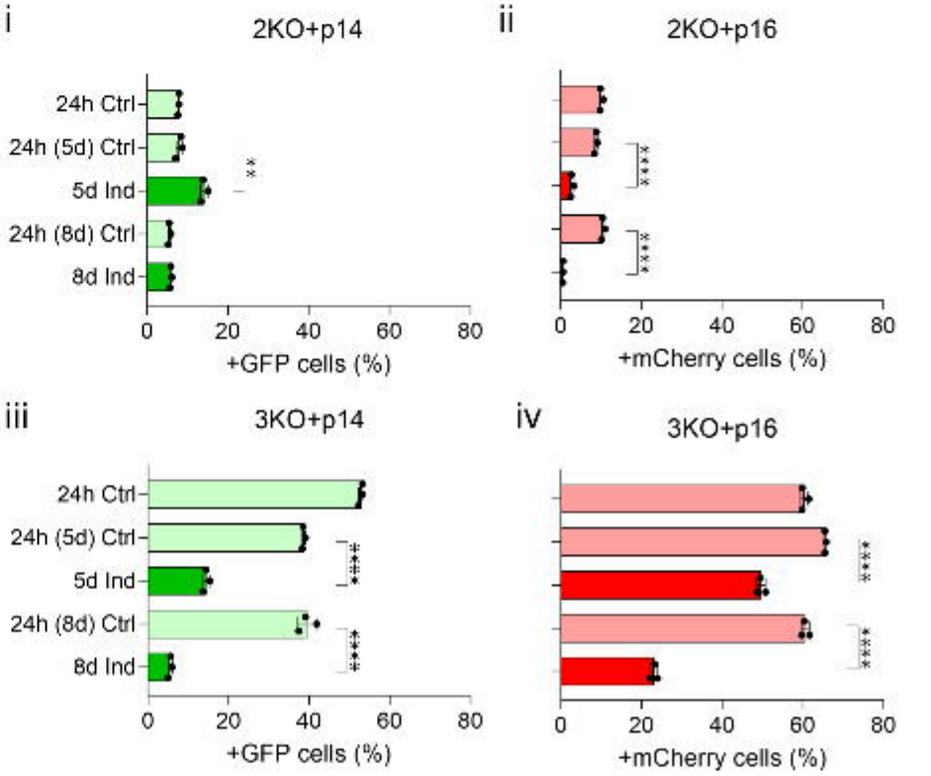

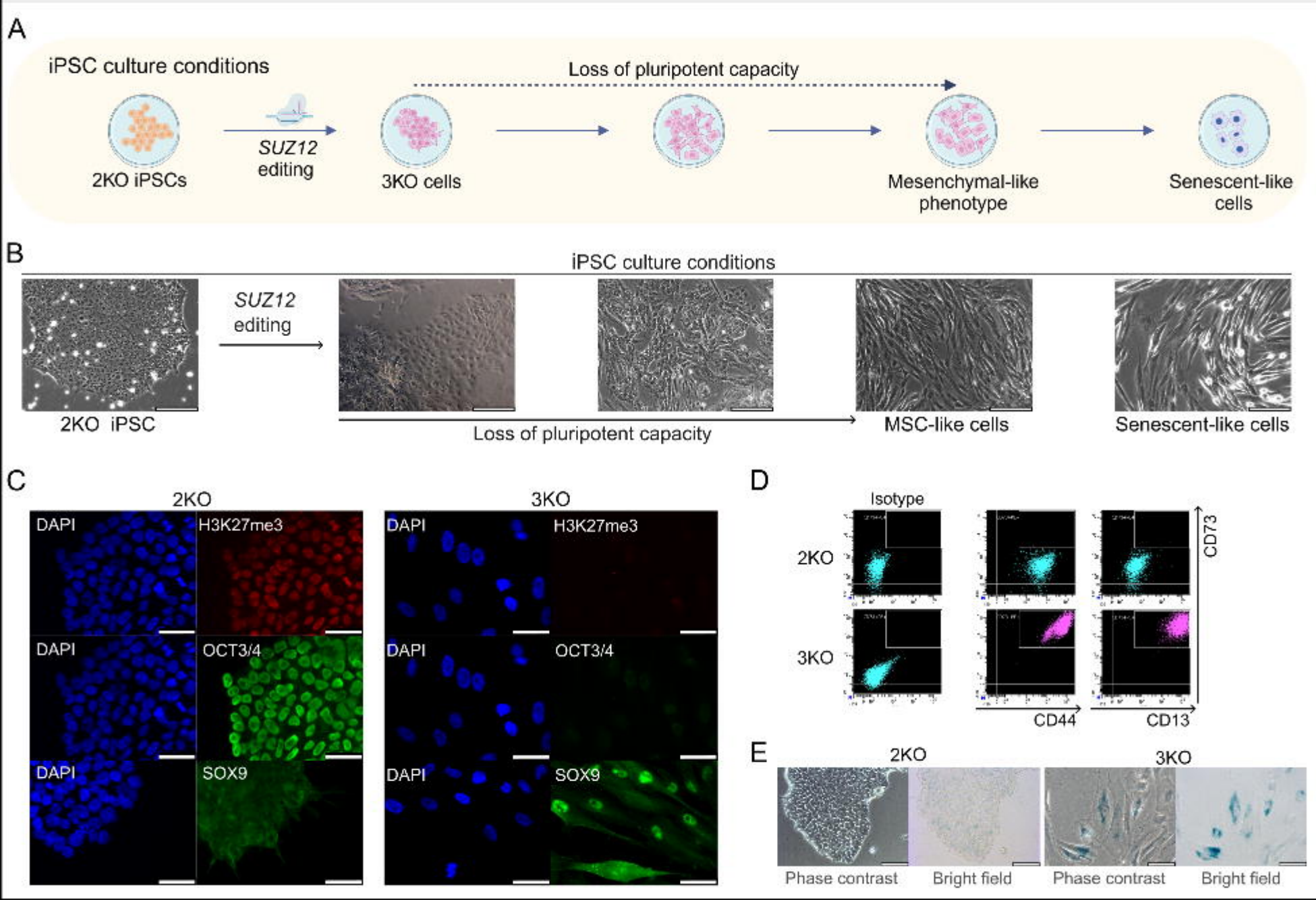
A
iPSC culture conditions
Loss of pluripotent capacity
2KO iPSCs
SUZ12 editing
3KO cells
Mesenchymal-like phenotype
Senescent-like cells
B
iPSC culture conditions
SUZ12 editing
2KO iPSC
Loss of pluripotent capacity
MSC-like cells
Senescent-like cells
C
2KO
3KO
DAPI
H3K27me3
OCT3/4
SOX9
D
Isotype
2KO
3KO
CD73
CD44
CD13
E
2KO
3KO
Phase contrast
Bright field
Phase contrast
Bright field

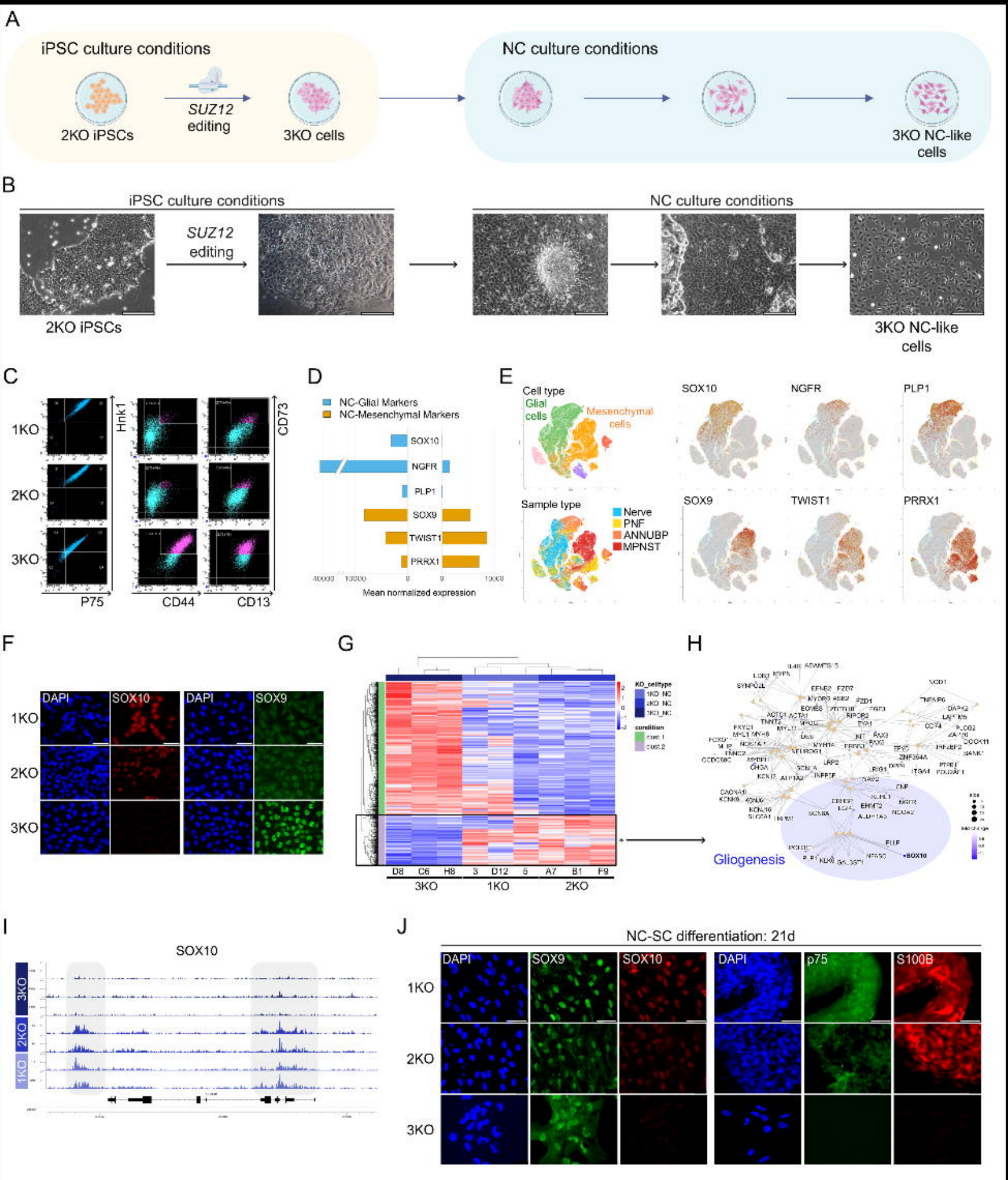
A
iPSC culture conditions
2KO iPSCs
SUZ12 editing
3KO cells
NC culture conditions
3KO NC-like cells
B
iPSC culture conditions
NC culture conditions
SUZ12 editing
2KO iPSCs
3KO NC-like cells
C
1KO
2KO
3KO
Hnk1
CD73
P75
CD44
CD13
D
NC-Glial Markers
NC-Mesenchymal Markers
SOX10
NGFR
PLP1
SOX9
TWIST1
PRRX1
Mean normalized expression
E
Cell type
Glial cells
Mesenchymal cells
Sample type
Nerve
PNF
ANNUBP
MPNST
SOX10
NGFR
PLP1
SOX9
TWIST1
PRRX1
F
DAPI
SOX10
DAPI
SOX9
1KO
2KO
3KO
G
KO_celltype
condition
D8
C6
H8
3
D12
5
A7
B1
F9
3KO
1KO
2KO
H
Gliogenesis
I
SOX10
3KO
2KO
1KO
J
NC-SC differentiation: 21d
DAPI
SOX9
SOX10
DAPI
p75
S100B
1KO
2KO
3KO

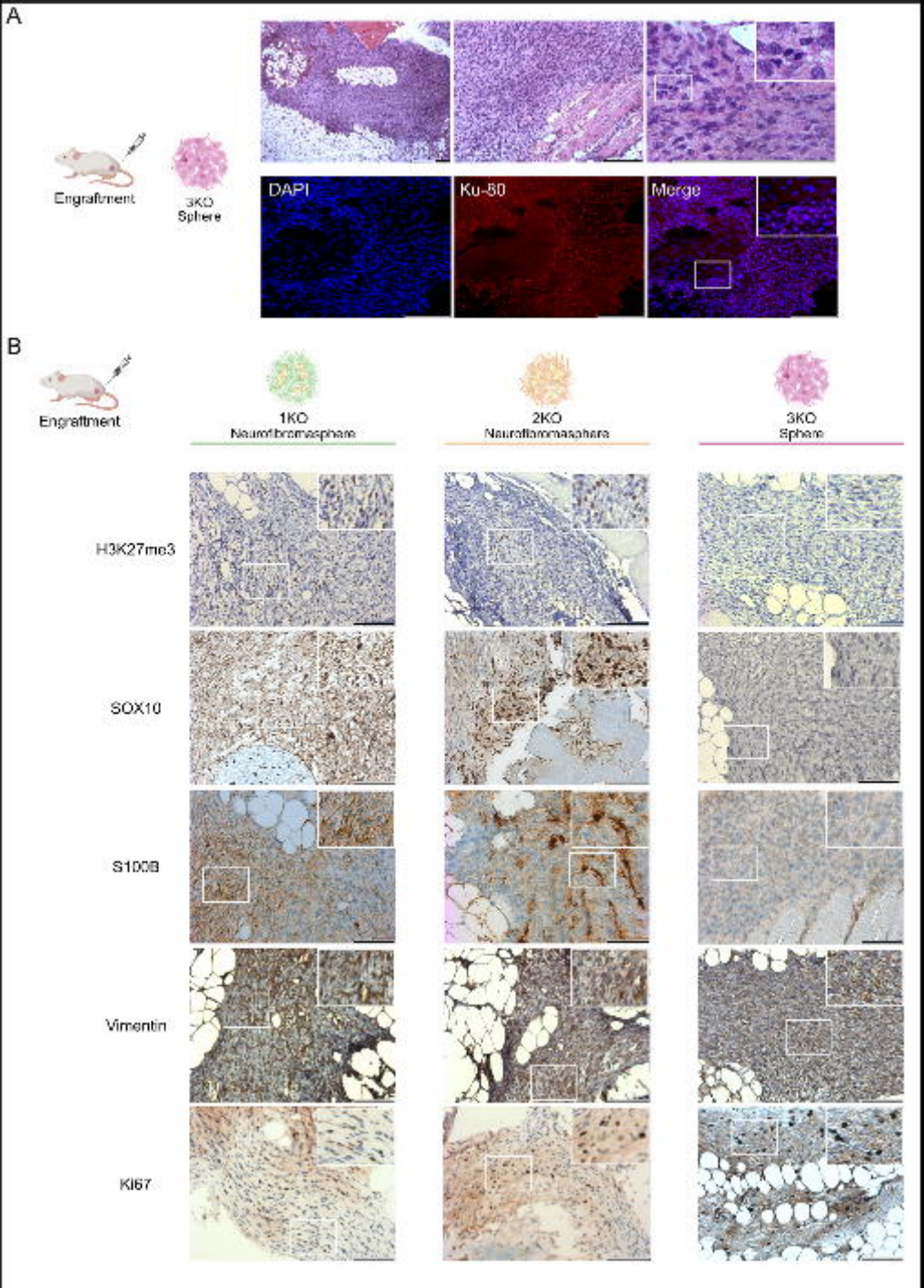
A
Engraftment
3KO
Sphere
DAPI
Ku-80
Merge
B
Engraftment
1KO
Neurofibromasphere
2KO
Neurofibromasphere
3KO
Sphere
H3K27me3
SOX10
S100B
Vimentin
Ki67

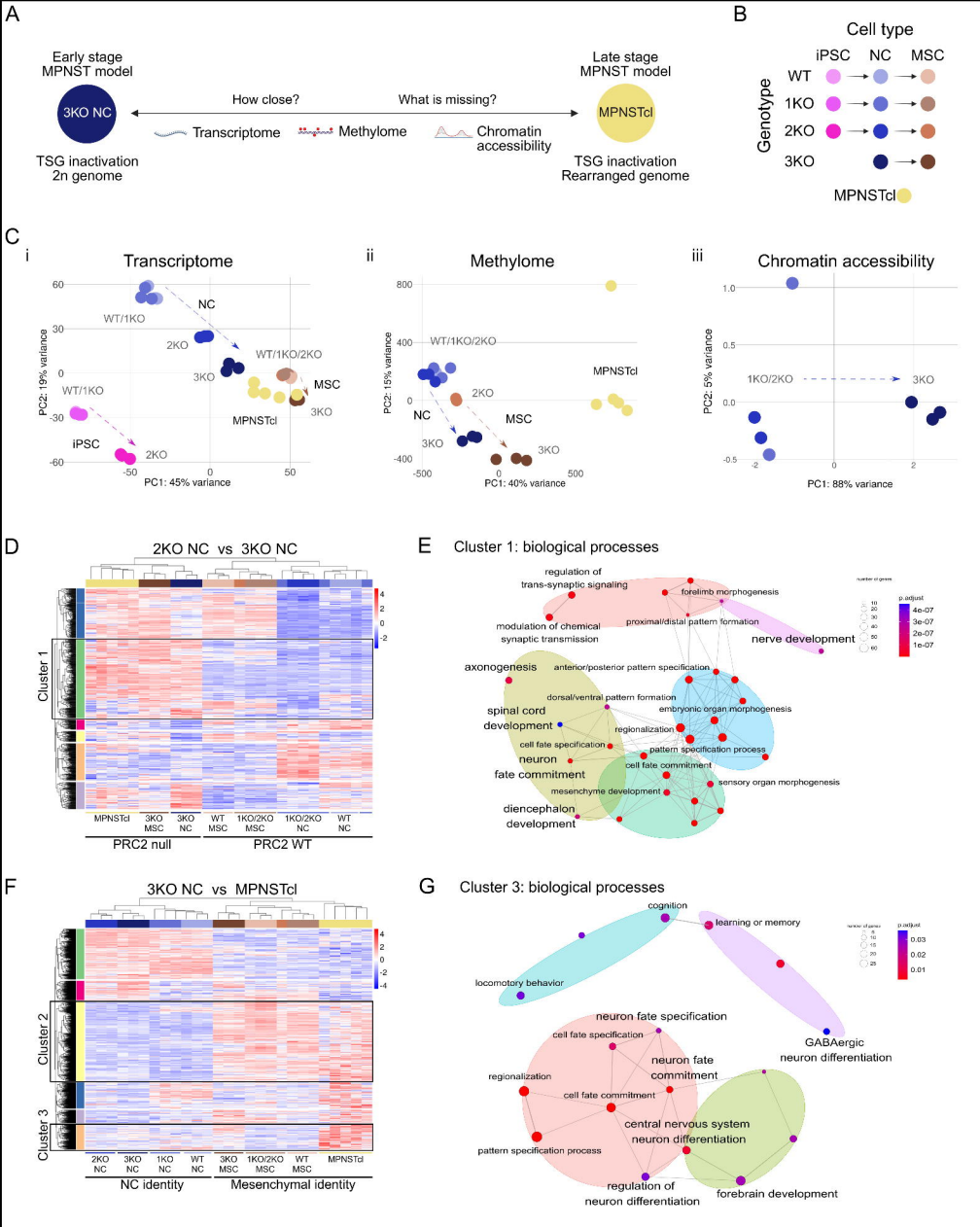
A
Early stage MPNST model
3KO NC
TSG inactivation
2n genome
How close?
What is missing?
Transcriptome
Methylome
Chromatin accessibility
Late stage MPNST model
MPNSTcl
TSG inactivation
Rearranged genome
B
Cell type
iPSC
NC
MSC
Genotype
WT
1KO
2KO
3KO
MPNSTcl
C
i
Transcriptome
PC2: 19% variance
PC1: 45% variance
WT/1KO
NC
2KO
WT/1KO/2KO
3KO
MSC
MPNSTcl
iPSC
ii
Methylome
PC2: 15% variance
PC1: 40% variance
WT/1KO/2KO
MPNSTcl
2KO
NC
MSC
3KO
iii
Chromatin accessibility
PC2: 5% variance
PC1: 88% variance
1KO/2KO
3KO
D
2KO NC vs 3KO NC
Cluster 1
MPNSTcl
3KO MSC
3KO NC
WT MSC
1KO/2KO MSC
1KO/2KO NC
WT NC
PRC2 null
PRC2 WT
E
Cluster 1: biological processes
regulation of trans-synaptic signaling
forelimb morphogenesis
modulation of chemical synaptic transmission
proximal/distal pattern formation
nerve development
axonogenesis
anterior/posterior pattern specification
dorsal/ventral pattern formation
embryonic organ morphogenesis
spinal cord development
regionalization
cell fate specification
pattern specification process
neuron fate commitment
cell fate commitment
sensory organ morphogenesis
mesenchyme development
diencephalon development
number of genes
p.adjust
F
3KO NC vs MPNSTcl
Cluster 2
Cluster 3
2KO NC
3KO NC
1KO NC
WT NC
3KO MSC
1KO/2KO MSC
WT MSC
MPNSTcl
NC identity
Mesenchymal identity
G
Cluster 3: biological processes
cognition
learning or memory
locomotory behavior
neuron fate specification
cell fate specification
GABAergic neuron differentiation
neuron fate commitment
regionalization
cell fate commitment
central nervous system neuron differentiation
pattern specification process
regulation of neuron differentiation
forebrain development
number of genes
p.adjust

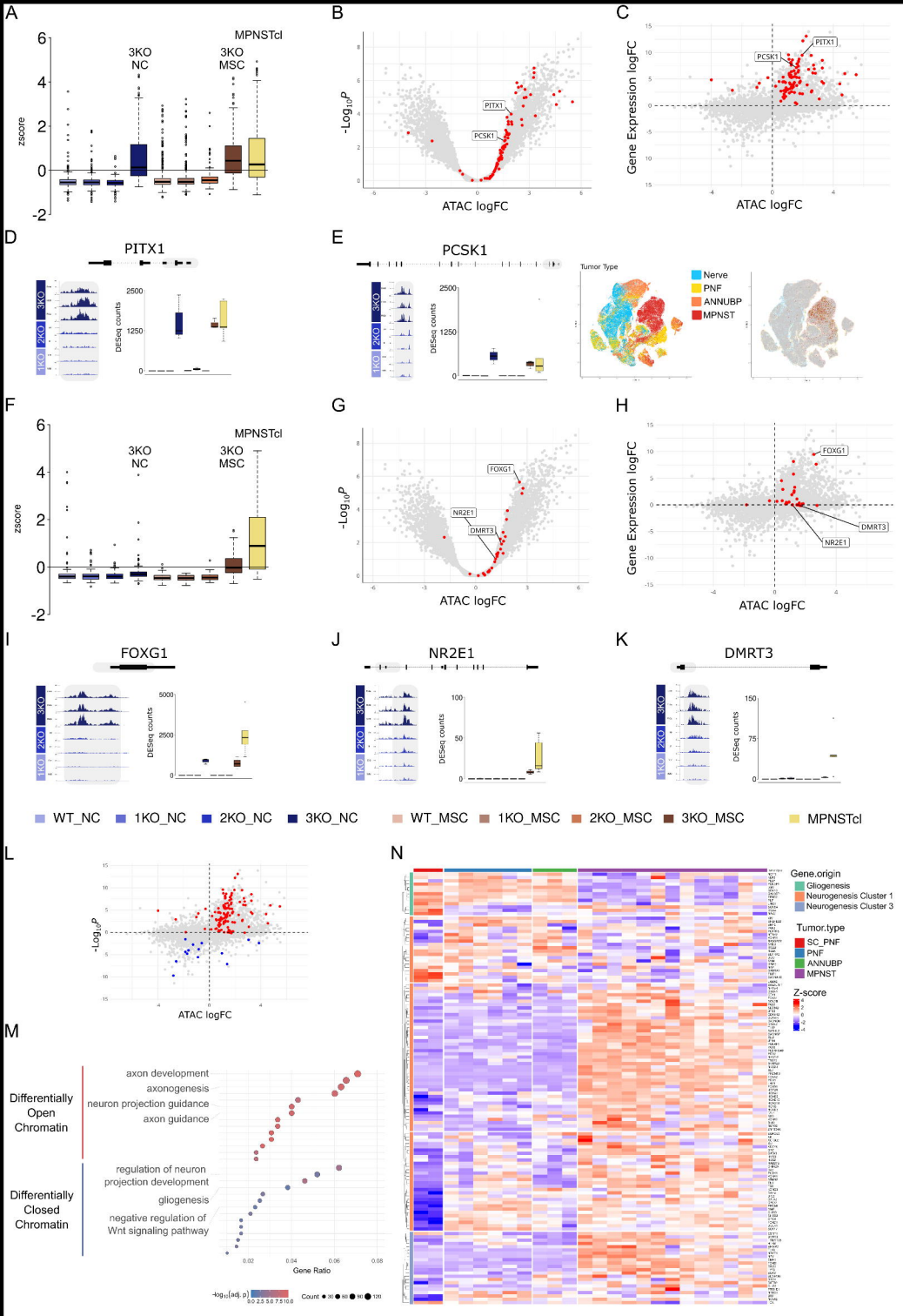
A
MPNSTcl
3KO NC
3KO MSC
zscore
B
-Log10P
PITX1
PCSK1
ATAC logFC
C
Gene Expression logFC
PITX1
PCSK1
ATAC logFC
D
PITX1
3KO
2KO
1KO
DESeq counts
E
PCSK1
Tumor Type
Nerve
PNF
ANNUBP
MPNST
F
MPNSTcl
3KO NC
3KO MSC
zscore
G
-Log10P
FOXG1
NR2E1
DMRT3
ATAC logFC
H
Gene Expression logFC
FOXG1
DMRT3
NR2E1
ATAC logFC
I
FOXG1
J
NR2E1
K
DMRT3
WT_NC
1KO_NC
2KO_NC
3KO_NC
WT_MSC
1KO_MSC
2KO_MSC
3KO_MSC
MPNSTcl
L
-Log10P
ATAC logFC
M
Differentially Open Chromatin
axon development
axonogenesis
neuron projection guidance
axon guidance
Differentially Closed Chromatin
regulation of neuron projection development
gliogenesis
negative regulation of Wnt signaling pathway
Gene Ratio
-log10(adj. p)
Count
N
Gene.origin
Gliogenesis
Neurogenesis Cluster 1
Neurogenesis Cluster 3
Tumor.type
SC_PNF
PNF
ANNUBP
MPNST
Z-score

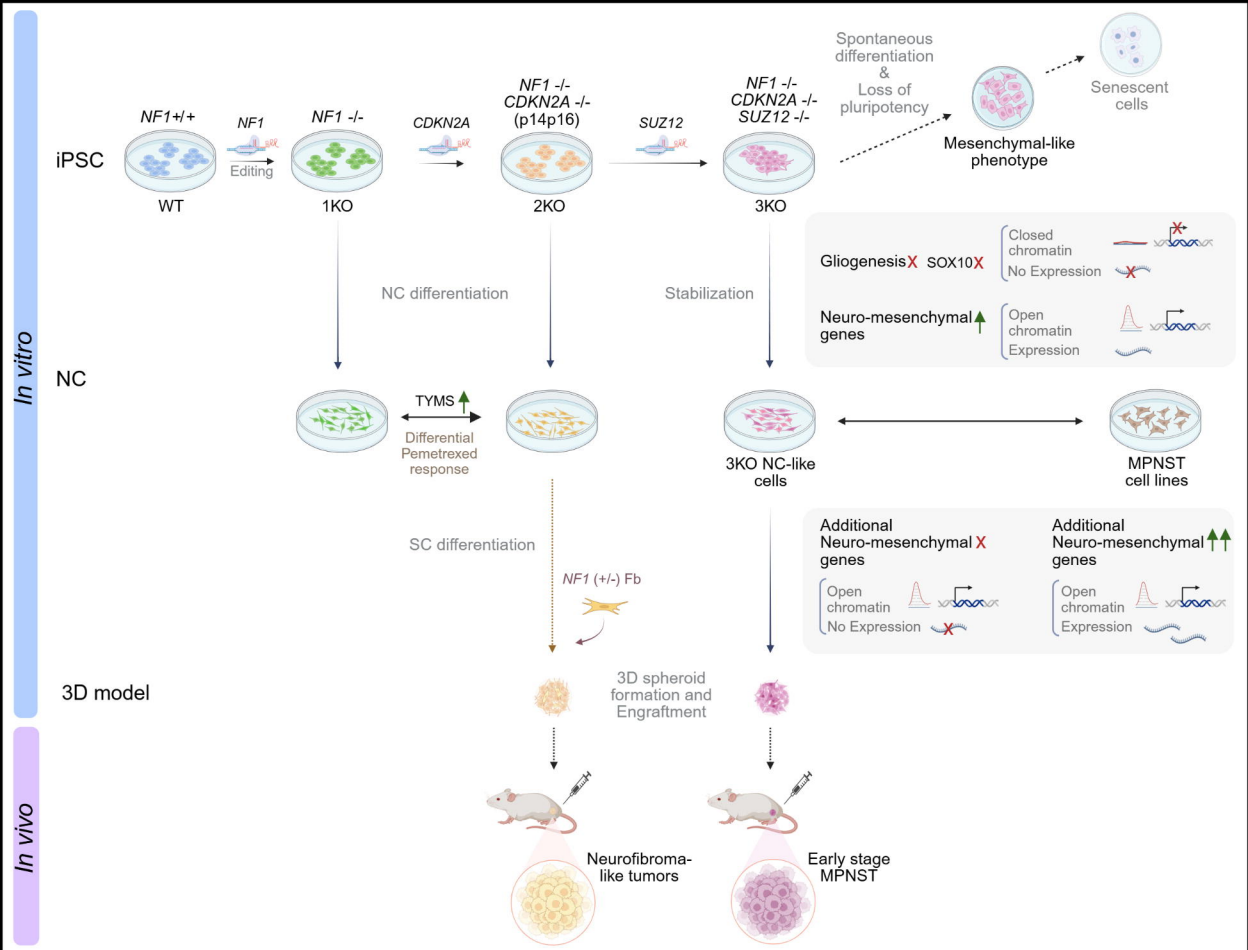
In vitro
In vivo
iPSC
NF1+/+
WT
NF1
Editing
NF1 -/-
1KO
CDKN2A
NF1 -/-
CDKN2A -/-
(p14p16)
2KO
SUZ12
NF1 -/-
CDKN2A -/-
SUZ12 -/-
3KO
Spontaneous differentiation & Loss of pluripotency
Mesenchymal-like phenotype
Senescent cells
NC differentiation
Stabilization
Gliogenesis X
SOX10 X
Closed chromatin
No Expression
Neuro-mesenchymal genes
Open chromatin
Expression
NC
TYMS
Differential Pemetrexed response
3KO NC-like cells
MPNST cell lines
SC differentiation
NF1 (+/-) Fb
Additional Neuro-mesenchymal genes X
Open chromatin
No Expression
Additional Neuro-mesenchymal genes
Open chromatin
Expression
3D model
3D spheroid formation and Engraftment
Neurofibroma-like tumors
Early stage MPNST